Angewandte Chemie
Eine Zeitschrift der Gesellschaft Deutscher Chemiker

Supporting Information

Beweis von Schwefel-non-Innocence in [Co^{II}(Dithiacyclam)]$^{2+}$-vermittelten, katalytischen Sauerstoff-Reduktions-Reaktionen

B. Battistella, L. Iffland-Mühlhaus, M. Schütze, B. Cula, U. Kuhlmann, H. Dau, P. Hildebrandt, T. Lohmiller, S. Mebs, U.-P. Apfel, K. Ray**

Table of contents

1. Experimental Section

I. Materials

Chemicals and handling. The chemicals employed were purchased from the company SIGMA ALDRICH and used without further purification. Anhydrous solvents were purchased from CARL-ROTH GmbH (acetonitrile, diethyl ether, dichloromethane) and Fischer Scientific Ltd (acetone) under the tradename ROTIDRY (>99.5%, <50 ppm H_2O), degassed prior to use and stored over activated molecular sieves. Deuterated solvents were purchased from EURISO-TOP.
Preparation and handling of air or water sensitive compounds were performed under an inert atmosphere using either Schlenk techniques or a GS MEGA glovebox from GS-GLOVEBOX Systemtechnik GmbH filled with N_2. Nitrogen and argon of quality 5.0 were used for this purpose and were purchased from AIR LIQUIDE.

II. Instrumentation and Physical Methods

Elemental analysis. All elemental analyses were performed by the analytical service of the Institut für Chemie of the Humboldt-Universität zu Berlin. The percentages of Carbon, Hydrogen, Nitrogen and Sulfur were determined using an HEKAtech EURO EA 3000 analyzer. The reported values are the result of an average of two independent measurements.

Nuclear magnetic resonance spectroscopy. All NMR spectra were recorded using a BRUKER 300 DPX spectrometer equipped with a cryostat. ^{1}H NMR were recorded in deuterated solvents, and chemical shifts (ppm) referenced against residual protic solvent peaks.

Electrospray ionization mass spectrometry. ESI-MS spectrum of **2-*cis*** (TFA^- coordinated) in solution was recorded by using an AGILENT TECHNOLOGIES 1200 MASS spectrometer; acetonitrile was used as an eluent and the sample was directly injected into the instruments from freshly thawed solutions. The analysis of the data was carried out with the ADVION DATA EXPRESS Version 6.0.11.3 or MestReNova software.

Single crystal X-ray structure determinations. For the determination of the X-ray molecular structure of the complexes data collection was performed at 100 K on a BRUKER D8 VENTURE diffractometer by using Mo Kα radiation (λ = 0.71073 Å), or at 100 K on a Rigaku Oxford diffraction XtraLAB Synergy-S with a HyPix-6000HE detector (Cu Kα radiation, λ = 1.54184 Å). Multi-scan absorption corrections implemented in SADABS[1] were applied to the data or obtained data were analyzed using the CrysAlis^{Pro} software package. The structures were solved by direct methods (ShelXS)[2] or intrinsic phasing (SHELXT 2014/5)[3] and refined by full matrix least square procedures based on F^2 with all measured reflections (SHELXL-2018/3)[4] in the graphical user interface SHELXle[5] with anisotropic temperature factors for all non-hydrogen atoms. All hydrogen atoms were added geometrically and refined by using a riding model. CCDC deposition number 2193635 contains the supplementary

crystallographic data for this paper. These data can be obtained free of charge from the Cambridge Crystallographic Data Centre via www.ccdc.cam.ac.uk/data_request/cif.

X-ray absorption spectroscopy. XAS at the Co K-edge was performed at beamline KMC-3 at the BESSY-II synchrotron (Helmholtz Center Berlin, Germany) using a set-up including a Si[111] double-crystal monochromator, a 13-element energy-resolving Si-drift detector (RaySpec) for X-ray fluorescence monitoring, and DXP-XMAP pulse-processing electronics (XIA). Samples were held at 20 K in a liquid-helium cryostat (Oxford). The energy axis of the monochromator was calibrated (accuracy ±0.1 eV) using the K-edge spectrum of 7709 eV. The spot size on the samples was ca. 1.5 x 3.0 mm (vertical x horizontal) as set by a focusing mirror and slits. X-ray fluorescence spectra were collected using a continuous scan mode of the monochromator (scan duration ~10 min). Up to 6 scans were averaged (1-2 scans per sample spot) for signal-to-noise ratio improvement. XAS data were processed (dead-time correction, background subtraction, normalization) to yield XANES and EXAFS spectra using our earlier described procedures and in-house software.[6–8] k^3-weighted EXAFS spectra were simulated with in-house software and phase functions from FEFF9 (S0 2 = 1.0).[9] EXAFS simulation results are tabulated in Tables S3-4.

UV–vis absorption spectroscopy experiment and data analysis. The UV–vis absorption spectra were recorded with a 8453 UV-visible Spectroscopy system from Agilent with argon purging. The measurements were carried out in 10 mm or 5 mm precision cuvettes made of SUPRASIL® quartz glass, the closures of which were equipped with a septum. The measurements at low temperatures were carried out by cooling the cuvette holder using a cooling thermostat USP-203-A from Unisoku Scientific Instruments. The analysis of the spectra was carried out with the software UV–visible Chemstation from Agilent. For a typical UV–vis experiment, a complex solution (2 mL or 1 mL) of known concentration was prepared in the glove-box and transferred into a cuvette. The cuvette was then placed in the thermostat and the measurement was started once the solution was in thermal equilibrium with the cryostat environment. A small argon stream was constantly maintained in the cuvette through the septum on top of the solution to prevent any oxygen interferences with the monitored reactions when required. The solutions of the different reactants were prepared in a minimum amount of solvent and then injected into the cuvette through the septum using air-tight syringes. The changes in the UV–vis spectrum were then recorded. The specified molar extinction coefficients ($\boldsymbol{\varepsilon}$) of the specific absorption maxima ($\boldsymbol{\lambda_{max}}$) are mean values of several individual measurements. The lifetime ($t_{½}$) of the intermediates was determined by following the decrease in the specific absorption band of the species over time at a certain temperature. The kinetics of decay were determined analogously, by following the decrease in the absorption bands.

Resonance Raman (rRaman). Resonance Raman spectra were measured in acetone, acetone-d_6 and DCM at –70 °C (Bruker cryostat) with 406 nm excitation from Kr^+-laser (Coherent) at 5 mW power and in MeCN and MeCN-d_3 using 514 nm excitation (Coherent) employing a Horiba Jobin-Yvon LabRAM HR800 confocal Raman spectrometer. The sample concentrations were 8 mM. Single isotope labelling experiment was performed by using a statistical mixture of $^{16}O_2$, $^{16}O^{18}O$, and $^{18}O_2$ in 1:2:1 ratio, generated by applying a high voltage via Tesla gun to a Young flask containing 1:1 $^{16}O_2/^{18}O_2$ mixture;[10] product formation was confirmed by Gas Chromatography (GC).

Electron paramagnetic resonance (EPR). EPR spectra were collected on a Bruker EMXplus instrument at a frequency of ca. 9.35 GHz (X-Band) in perpendicular mode. All samples were measured at a temperature of ~13 K as frozen solutions (powder-like spectra) by the use of a liquid helium recirculating cooling system (ColdEdge). EPR spectral simulations were performed using *EasySpin* (version 5.2.35).[11] Simulations for the high-spin Co^{II} (S = 3/2) systems were, due to the lack of knowledge about the zero-field splitting parameters *D* and *E*, performed based on an effective spin S^{eff} = 1/2, providing effective g^{eff} and A^{eff} parameters. The yields of **1a** and **2a** in the reaction of **1** and **2** towards dioxygen were determined by spin quantification, comparing the relative spectral intensities

through double integration of the derivative-like EPR signals of **1** and **1a**, respectively **2** and **2a**, when **1a** and **2a** were generated from the exact same solution of the corresponding starting compound (no variation in the Co concentration). To account for the impact of the different *g* values on the signal intensities,[12] the individual spectral intensities were referenced with regard to the respective unscaled simulated signals, which *EasySpin* calculates based on the same number of spins for each compound. The obtained relative scaling factors (1/1 for **1**/**1a** and 1/1.51 for **2**/**2a**) were then considered in the quantification.

Cyclic voltammetry (CV). All CV experiments were performed with a PalmSens3 or PalmSens4 potentiostat. The supporting electrolyte for all electrochemical experiments in organic solvents was tetrabutylammonium hexafluorophosphate ($[(^nBu)_4N]PF_6$, 0.1 M). All CV measurements were performed in three electrode setup using a glassy carbon working electrode, a platinum wire counter electrode and a silver wire pseudo reference. The working electrode was prepared by successive polishing and subsequent sonication in the applied solvent for 10 min prior to its use. If not otherwise mentioned, all experiments were performed under inert argon atmosphere. All pseudo-referenced potentials were referenced against the ferrocene/ferrocenium redox potential ($Fc^{+/0}$).

III. Syntheses

Synthesis of [Co(S_2N_2-cyclam)$(TFA)_2$] (2-*cis*).

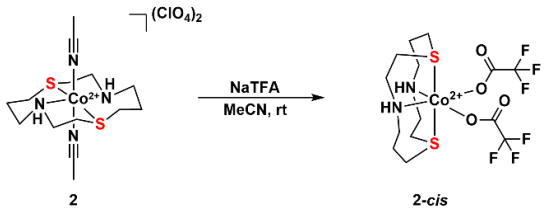

2 2-*cis*

Compound **2** (20 mg, 0.03 mmol) was dissolved under inert atmosphere in MeCN (5 mL) and 5 equiv. sodium trifluoroacetate (23.7 mg, 0.17 mmol) were added. The reaction mixture was stirred for 2 h at 25 °C while a color change from red to pink was observed. After the volume of the solvent was reduced by half under reduced pressure, the reaction mixture was filtered by silica column using MeCN as eluent. Subsequently, the solution volume was reduced by half and from the concentrated complex solution **2-*cis*** was obtained as crystalline material in 63% (11 mg, 0.02 mmol) yield (Tables S7-8). ESI-MS: calcd. for $C_{12}H_{22}CoF_3N_2O_2S_2$ *m/z* = 406.040 $[Co(L)(F_3CCO_2)]^+$ and $C_{10}H_{21}CoN_2S_2$ *m/z* = 292.048 $[Co(L-H)]^+$; found: *m/z* = 406.038 and 292.044.

IV. Generation of the intermediates and sample preparation

Generation of Co(III)-superoxo (1a) and $Co(III)_2$-1,2-μ-peroxo (1b) in 1-O_2. In a typical experiment acetone (1.9 mL) was cooled to –70 °C and saturated with O_2 by bubbling it from a balloon into the solution for 2 minutes. To this solution a pale-yellow solution of **1** in acetone (20 mM, 0.1 mL) was injected and the formation of the ochre yellow intermediate **1-O_2** was monitored following the λ_{max} = 455 nm by UV-vis spectroscopy. For further spectroscopic studies the intermediate was generated in higher concentrations (rR and XAS: 8 mM).

Generation of Co(III)-peroxo (2a) and $Co(III)_2$-1,2-μ-peroxo (2b) in 2-O_2. In a typical experiment MeCN (1.9 mL) was cooled to –30 °C and saturated with O_2 by bubbling it from a balloon in the solution for 2 minutes. To this solution a pale pink solution of **2** in MeCN (20 mM, 0.1 mL) was injected and the formation of the red intermediate **2-O_2** was monitored following the λ_{max} = 695 nm by UV-vis spectroscopy. For further spectroscopic studies the intermediate was generated in higher concentrations (rR and XAS: 8 mM).

Preparation of the $^{18}O_2$-enriched sample for rR spectroscopy. A 8 mM solution of **1** in DCM, acetone or acetone-d_6 and **2** in MeCN-d_3 under inert atmosphere was cooled to respectively –70 °C or –35 °C and $^{18}O_2$ was bubbled gently from a balloon through the solution for 1 minute. The formation of **1a**/**1b** and **2a**/**2b** was monitored by the growth of their characteristic optical features, before freezing aliquots of the solutions into standard NMR tubes. The same procedure was employed in the preparation of the single isotope labeled **2a**/**2b** from a 8 mM MeCN-d_3 solution of **2**.

V. Catalytic Oxygen Reduction

Evaluation of the Catalytic activity of 1 and 2 in ORR. The evaluation of the catalytic activity of **1** and **2** towards dioxygen reduction was carried out using the Fukuzumi and Guilard's method:[13] decamethylferrocene (Fc*) was employed as one-electron donor, trifluoroacetic acid (TFA) was used as proton sources and in their presence O_2 was set to react with a catalytic amount of **1** and **2** (respectively in acetone or MeCN) at 25 °C. The occurrence of the oxygen reduction reaction was proved by the formation of decamethylferrocenium ion (Fc^{*+}) with characteristic absorption band (Fc^{*+}: λ_{max} = 780 nm, ε = 520 M^{-1} cm^{-1} in acetone; Fc^{*+}: λ_{max}= 778 nm, ε = 488 $M^{-1}cm^{-1}$ in MeCN).[14–19] When employing ferrocene (Fc) as reductant (3 mM) in the presence of TFA (10 mM) and **1** or **2** as a catalyst (0.1 mM) in acetonitrile solution saturated with O_2 (12.1 mM) at 25 °C, oxygen reduction took place, as evidenced by the formation of ferrocenium ion (Fc^+) in solution (Figure 1 in the main text). Blank reaction performed under the same experimental conditions showed no formation of Fc^+ in absence of **1** or **2** after 90 minutes and iodometric titration (see below) confirmed no H_2O_2 generation in the reaction (Figure S3). Nevertheless, the instability of Fc^+ in presence of an excess of O_2 and TFA in solution, makes the use of the stronger reductant Fc* most favorable for the catalytic ORR study, due to the higher Fc^{*+} stability in an O_2 saturated solution in acidic environment.[20] Therefore, more detailed investigation of the reaction products and selectivity has been performed employing Fc* as electron donor. When Fc* was used, the formation of Fc^{*+} could be detected and monitored by a rise in absorbance at 780, which indicated that the oxidation of Fc* took place with the concomitant O_2 reduction in the presence of **1** and **2** as a catalysts.[15] Since Fc* is known to be oxidized by O_2 in acidic environment, blank reactions were taken into consideration while determining the catalytic capacity of the system.

Iodometric titration for the determination of H_2O_2. The amount of H_2O_2 was determined by titration with iodide ion, as described previously in the literature.[14,19,21–23] In the iodometric titration, the formation of I_3^- and the consumption of H_2O_2 follows a one-to-one ratio (3 NaI + H_2O_2 + 2 H^+ → I_3^- + 3 Na^+ + 2 H_2O).[14,19,21] The concentration of H_2O_2 can be derived from the concentration of I_3^- by the Beer-Lambert law according to the equation:

$$\text{Abs at } \lambda_{max} \text{ 361 nm} = \varepsilon \cdot b \cdot [I_3^-]$$

where ε = $2.8 \cdot 10^4$ M^{-1} cm^{-1} and b = optical path length. All iodometric titrations are conducted anaerobically to avoid the oxidation of I^- to I_3^- by O_2. A 100 μL aliquot of the 2 mL catalytic reaction mixture was diluted in MeCN (1.90 mL) containing an excess amount of NaI (0.1 M). The amount of I_3^- formed was determined by UV-visible absorption spectroscopy at λ_{max} = 361 nm[14,19,21]. The absorbance at 361 nm was compared to the absorbance of 0.1 M solution of NaI without addition of the reaction mixture (Figure 1 insets, Figure S4-5). The difference in the absorbance at 361 nm was used to quantify the amount of H_2O_2 formed in the catalytic reaction on the base of the limiting reagent (Fc or Fc*), considering:

- Maximal content of hydrogen peroxide produced considering 100% conversion of the reductant (Fc or Fc*) in the diluted reaction mixture solution: $[H_2O_2]$ (mM) = (0.1 mL/2.0 mL) · 1.5 mM = 0.075 mM.
- Abs at λ_{max} = 361 nm (NaI + reaction mixture) - Abs at λ_{max}=361 nm (NaI) = $\varepsilon \cdot 1$ cm $\cdot [I_3^-]$
- $[I_3^-] = [H_2O_2]$
- $([H_2O_2]/0.075 \text{ mM}) \cdot 100$ = selectivity (%)

^{1}H NMR H_2O_2 detection. The ^{1}H NMR spectrum of the reaction mixture of **1** and **2** (0.1 mM), Fc* (3 mM in DCM-d_2), TFA (10 mM) and O_2 (12.1 mM) at 25 °C in MeCN-d_3 was measured at 20 °C, as well as the ones of authentic samples containing a known amount of H_2O (3 mM), H_2O_2 (0-2.1 mM) and TFA (10 mM, to exclude the presence of water in both deuterated solvent and acid). The ^{1}H NMR spectra of the reaction mixtures show no traces of water in the ORR catalyzed by **1** and **2**. A signal at around 10.5 ppm was detected in both cases, ascribable to H_2O_2 in a MeCN solvated system where all the protons are hydrogen-bonded to each other, as previously reported in literature for similar systems (Figure S6).[24]

O_2/Fc* titration for mechanistic insight into ORR catalyzed by 1 and 2. Depending on the ORR mechanism, two- or four-electron O_2 reduction can be catalyzed by transition metal complexes[14,25]. When Fc* is used as one-electron donor, two or four equiv. Fc* are consumed depending on the process and determination of Fc^{*+} concentration after complete O_2 reduction can provide information about the reaction mechanism. On this basis, an O_2 titration experiment limiting the applied oxygen concentration in presence of an excess of Fc* was performed. The concentration of Fc^{*+} was calculated from the absorbance at 780 nm using the Beer-Lambert law, knowing the molar extinction coefficient ε=488 $M^{-1}cm^{-1}$[15]. Under inert atmosphere, MeCN solutions with known concentrations of of **1** and **2** together with Fc* were prepared and to these solutions aliquots of O_2-saturated acetonitrile solutions were added to achieve different O_2 concentrations. The dioxygen concentration in a O_2 saturated MeCN solution was considered 12.1 mM, estimating the solubility of pure oxygen in the solvent to be roughly 5 times higher than that of O_2 from air[26]. After addition of a known amount of TFA, the solution was vigorously shaken and the reaction monitored by following the UV-visible spectroscopic feature at λ_{max}=780 nm, until no spectral change was observed. Based on the final absorbance at λ_{max}=780 nm the concentration of Fc^{*+} was calculated. The final solutions (2 mL) consisted of 3 µM **1** or **2**, 3.63 mM Fc*, 20 mM TFA and O_2 (0.15, 0.3, 0.45, 0.6 and 1.2 mM). The calculated Fc^{*+} concentration was then plotted against O_2 concentration and the slope obtained by linear regression of the experimental points results in a 1:≈2 ratio between O_2:Fc^{*+} for both **1** and **2**, indicating a two-electron ORR mechanism (Figure S6).

Turnover Frequency determination for the $2e^-/2H^+$ reduction of O_2 by 1 and 2. According to the method proposed by Mayer and Stahl *et al.*, a background concentration of H_2O_2 (0.1 mM urea·H_2O_2) was added to each of the reactions to enable estimation of the equilibrium reduction potential of O_2 to H_2O_2 under catalytic conditions, since control experiments showed that excess of urea present in urea·H_2O_2 does not influence the rate of the reaction in the range 0.1-1 mM.[25] TFA is needed in the catalytic reaction because protons are consumed in the catalytic reduction of O_2, and the presence of *"buffer"* ensures that there are no large changes in the proton concentration during the course of the catalytic reaction.[19] In addition, the buffered condition provides the basis for establishing the thermodynamic reduction potential of O_2/H_2O_2 via open-circuit-potential (OCP) measurements.[19,27]

- Catalytic O_2 reduction under *buffered* conditions in presence of H_2O_2.

A 1.7 mL MeCN solution of 0.12 mM urea·H_2O_2 was flushed with O_2 (bubbled from a balloon for 2 minutes) to prepare the O_2-saturated solution. To this solution, 0.1 mL N_2-saturated MeCN solution of complex **1** or **2** (final concentration 10 µM), 0.1 mL of 200 mM NaTFA/TFA solution and 0.1 mL of 20 mM Fc* solution in DCM were rapidly added under vigorously stirring and the absorbance @ 780 nm was monitored by UV-visible spectroscopy at 25 °C. Final concentrations of each substrate in the reaction: 1 mM Fc*, 10 μM cobalt complex, 10 mM of each TFA and NaTFA, 0.1 mM urea·H_2O_2 and 10.4 mM O_2.

- Blank reaction

A 1.8 mL MeCN solution of 0.12 mM urea·H_2O_2 was flushed with O_2 (bubbled from a balloon for 2 minutes) to prepare the O_2-saturated solution. To this solution, 0.1 mL of 200 mM NaTFA/TFA solution and 0.1 mL of 20 mM Fc* solution in DCM were rapidly added under vigorously stirring and the absorbance @ 780 nm was monitored by UV-visible spectroscopy at 25 °C.
Final concentrations of each substrate in the reaction:

1 mM Fc*, 10 mM of each TFA and NaTFA, 0.1 mM urea·H_2O_2 and 10.9 mM O_2.

- Calculations of turnover frequencies (TOFs) for the catalytic O_2 reduction.

Background O_2 reduction by Fc* was observed in the absence of cobalt catalysts under the experimental conditions (Figure S7-8, grey traces)[28] and the rate of this reaction was subtracted from the initial rates obtained from the reactions conducted in the presence of catalysts.[19] Initial rates (M s^{-1}) were obtained by fitting UV-visible time-course data with linear regression during the first ~10% of the reaction (insets in the plots, Figure S7-8). The turnover frequencies (TOFs, s^{-1}) were then determined by dividing the initial rate by two (to account for the two-electron stoichiometry in the conversion of O_2 to H_2O_2) and the catalyst concentration.
Under the above-mentioned experimental conditions, in the same way the TOFs for the two-electron O_2 reduction catalyzed by **1** and **2** were determined using acetone as solvent. TOFs for the ORR catalyzed by both **1** and **2** in both solvation environments are reported in Table S1.

Cyclic voltammograms (CV) under buffered conditions. For a correctly calculated effective overpotential for the catalytic O_2 reduction the actual $E_{1/2}(Co^{III/II})$ under catalytic conditions has to be considered. Half-wave potentials of **1** and **2** were recorded in presence of acid and conjugate base, since the catalytic rates of O_2 reduction were also measured under buffered conditions. In the catalytic cycle protons are consumed and thus, buffered conditions are used to ensure that there are only negligible changes in the proton concentration.[19,25] By performing CV analysis at different scan rate, linear dependence between peak current and square root of the scan rate was found for both **1** and **2** in the solvents of used (Figures S9-10). This linear dependence displayed the reversible behavior of the $Co^{III/II}$ redox couples and allowed determination of the $E_{1/2}(Co^{III/II})$ used for effective overpotential determination. The mean values of nine $Co^{III/II}$ half wave potential (determined at different scan rates) were used as $E_{1/2}(Co^{III/II})$ values for effective overpotential determination and are listed in Table S1. CV experiments were performed with a three-electrode setup including glassy carbon working electrode, Pt wire counter electrode and Ag wire as pseudo-reference electrode. As supporting electrolyte 0.1 M tetrabutylammonium hexafluorophosphate ($[(^nBu)_4N]PF_6$) was used and all cyclic voltammograms were referenced against the ferrocene/ferrocenium redox potential ($Fc^{+/0}$).

Open-circuit potential (OCP) measurements for $E_{H+/H2}$ with different buffered conditions. The H^+/H_2 potential in organic media was determined by open-circuit potential measurements at a Pt electrode using a recently reported protocol.[25,29] A schematic view of the four-electrode cell configuration is given in Figure S12. The Pt wire of the Pt electrode was conditioned prior to its use. For this purpose, the Pt wire was polished, washed with acetone and then immersed in fresh aqua regia for 30 min. After rinsing it with distilled water, the Pt wire was dried and handled under Ar. A separated Pt wire was used as counter electrode and Ag wire was employed as pseudo reference electrode. The resulting homogeneous solution composed by acid, its conjugate base and supporting electrolyte was analyzed, using Fc as a reference compound (Figure S12). After saturation of the solution with gaseous hydrogen a cyclic voltammogram spanning the reference couple was recorded using the glassy carbon working electrode, pseudo reference electrode and counter electrode. Afterwards the OCP between the pseudo reference electrode and the Pt wire electrode was measured, while stirring and continuously sparging the solution with hydrogen. OCP was measured for 60 s and measurements were repeated until a stable OCP trace was obtained (Figure S13). For all OCP measurements *buffered* conditions were used, because the presence of buffer ensure only negligible changes in the proton concentration during the OCP measurements of $E_{H+/H2}$.[19,25] The different experimental conditions for OCP measurements are summarized as follow:

Solvent	Acid	Base	Supporting electrolyte	Reference compound
MeCN	TFA (10 mM)	TFA^- (10 mM)	$[(^nBu)_4N]PF_6$ (0.1 M)	Fc
acetone	TFA (10 mM)	TFA^- (10 mM)	$[(^nBu)_4N]PF_6$ (0.1 M)	Fc

Estimation of $E_{O2/H2O2}$ based on $E_{H^+/H2}$ measured by OCP. For the estimation of the O_2/H_2O_2 reduction potential in organic media i) the standard aqueous cell potential for $O_2 + H_2 \rightarrow H_2O_2$, ii) the measurement of the H^+/H_2 ($E_{H+/H2}$) open-circuit potential (OCP) and iii) the Gibbs free energy to transfer H_2O_2 from H_2O into the organic media are used.[19] The solvation energy of H_2O_2 in the organic solvents of use is considered identical to that in H_2O and, therefore, is negligible.[30] Electrochemical measurements were carried out in presence of 10 mM TFA and 10 mM NaTFA in organic medium and $E_{O2/H2O2}$ was calculated by the following equations:

i)	$O_{2(g)} + H_{2(g)} \rightleftharpoons H_2O_{2(aq)}$	$E^\circ_{O_2/H_2O_2(aq)}$	= 0.68 V vs. $E_{H^+/H_2(aq)}$
ii)	$2\ H^+_{(CH_3CN)} + 2\ e^-_{(V\ vs.\ Fc^{+/0})} \rightleftharpoons H_{2(g)}$	$E_{H^+/H_2(CH_3CN)}$	= -0.636 V vs. $Fc^{+/0}$
	$2\ H^+_{(acetone)} + 2\ e^-_{(V\ vs.\ Fc^{+/0})} \rightleftharpoons H_{2(g)}$	$E_{H^+/H_2(acetone)}$	= -0.824 V vs. $Fc^{+/0}$
	$O_{2(g)} + 2\ e^-_{(V\ vs.\ Fc^{+/0})} + 2\ H^+_{(CH_3CN)} \rightleftharpoons H_2O_{2(CH_3CN)}$	**$E_{O_2/H_2O_2(CH_3CN)}$**	**= 0.044 V vs. $Fc^{+/0}$**
	$O_{2(g)} + 2\ e^-_{(V\ vs.\ Fc^{+/0})} + 2\ H^+_{(acetone)} \rightleftharpoons H_2O_{2(acetone)}$	**$E_{O_2/H_2O_2(acetone)}$**	**= -0.144 V vs. $Fc^{+/0}$**

As previously reported, the oxygen reduction catalyzed by **1** and **2** were conducted in the presence of 0.1 mM urea·H_2O_2 to establish a stable thermodynamic reference state for the effective overpotential. Because only a few of the previous published studies of catalytic ORR include a background concentration of H_2O_2 in the reaction medium, we elected not to use this reference state in the effective overpotentials reported here to ensure that all catalysts were treated the same way. Hence, the effective overpotentials were calculated by assuming the reactions were performed under standard-state conditions for the entire study (1 M H_2O_2) as reported elsewhere.[25]

2. Computational and theoretical methods

EXAFS fit and EXAFS-from-DFT. Analysis of the EXAFS spectra for **1**, **1a**/**1b** and **2**, **2a**/**2b** in solvated state was particularly complex due to mixtures of states in all four cases and because Co-N- and Co-C-shells overlap with Co-S-shells (Table S3). DFT calculations of potential structures computed on the basis of spectroscopic analysis of the species, provided reference coordination numbers and bond distances, which were used to deconvolute the experimental spectra (Table S3-4). In addition, EXAFS was calculated for the relaxed DFT structures using FEFF9, revealing notable differences in spectral shapes of related models. Pairwise weighted linear combinations of calculated EXAFS spectra proved to be helpful in disclosing the likely mixture compositions, further supporting the fits of the experimental EXAFS. The solution spectrum of **1** (**1**-solution) could be well represented by a 1:1 mixture of DFT-derived EXAFS **dft-1**, carrying two acetonitrile ligands and **dft-1'** (Figure S24b) carrying only one acetonitrile ligand (blue and light blue curves in Figure S18). This is in accordance with the fit of **1**-solution which strongly suggests the existence of one short Co-N contact at 2.12 Å (disregarding the four N ring-atoms at 1.95 Å) and one longer Co-N contact at 2.52 Å, hinting partial dispatchment of one acetonitrile ligand in acetone solution (Table S3). The Co(III)-superoxo **dft-1a** and the dimeric $Co(III)_2$-peroxo **dft-1b** (Figure 24c-d) exhibit almost identical coordination environments (see Table S3) and thus cannot be deconvoluted using EXAFS. Accordingly, the calculated EXAFS spectra also look very similar, and their 1:1 linear combination (orange line in Figure S18) is as good as the monomer or dimer lines (medium and light grey spectra in Figure S18) to describe the experimental **1a**/**1b** spectrum (red curve). Consistently, a 25%/75% ratio **1a**/**1b** could be experimentally established by EPR analysis (see main text). The pink and green lines in Figure S18 represent experimental and calculated *difference* spectra between solvated **1** and **1a**/**1b**, further supporting the validity of this approach. Despite these

issues, the oxidation state of **1**-solution resembles that of **1**-powder and shows a clear one-electron oxidation after treatment with O_2 in **1a**/**1b** (Figure S17). XAS data analysis became more complex for **2**, as XANES of the solvated sample (**2**-solution) indicates a structural change as well as a partial oxidation in comparison to **2**-powder (Figure S21). The powder spectrum is considerably curved and exhibits a shallow maximum, both indicating the presence of *softer* atoms (such as S) coordinated to Co as expected. After solvation, the XANES shape changes towards a steeper slope with a pronounced maximum, known for coordination environments with *harder* atoms (such as N or O), suggesting the partial dispatchment and diminished role of at least one S-atom. This was supported by the impossibility of fitting the experimental EXAFS spectrum with two S-shells at about 2.2 Å. DFT model **dft-2a**, containing a Co-O-O-S binding pattern (Scheme 2 in the main text, Figure S24f) has Co-S distances of about 2.4 and 3.2 Å, thus **2**-solution was fitted with three S-shells at about 2.3, 2.5, and 3.4 Å with the summed-up S-population (N) being fixed to two (restrained fit), suggesting a 1:1 mixture of the starting material and the oxidized **dft-2a** in **2-solution** (Figures 23, Tables S3-4). This was further supported applying corresponding EXAFS superpositions, i.e. a 1:1-mixture of **dft-2** (black) and **dft-2a** (dark grey): as can be seen in Figure S23, the light blue curve matches reasonably well with **2**-solution (blue). **2a**/**2b** was fitted assuming a roughly 1:1-mixture of **dft-2a** and **dft-2b** according to EPR spin quantification results (50% **2a** in **2a**/**2b** solution) and here the advance of this fit becomes particularly well visible, as both calculated spectra **dft-2a** and **dft-2b** do not match with the experimental one, whereas the 40%/60%-mixture matched quite good (orange and red lines in Figure S23). Furthermore, this approach results quite useful for the discriminations of the two isomeric forms of **2a** (*trans* and *cis*, Figure S24f-g). The two isomers result equally energetic according to DFT computations (Table S4) and thus, their simultaneous formation cannot be thermodynamically excluded. However, the computed EXAFS features for **2a-*cis*** are clearly counter phasic to the experimental data for **2a**/**2b** (Figure S23), hinting a negligible formation of **2a-*cis*** compare to the *trans* isomer **2a**.

Computational Methodology. Gas-phase structures for different states of **1** and **2** were obtained by DFT optimizations at the UB3PW91/6-311+G(2df,p)[31,32] level of theory applying Gaussian16.[33] The COSMO solvation model was used to mimic the acetone or acetonitrile solvation.[34] Dispersion was taken in account by the empirical dispersion correction of Grimme.[35] Subsequent normal mode analysis (frequency calculation) proved all structures to be minima on the potential energy hypersurface. The wavefunction file of **dft-1a** was used for a topological analysis of the electron density according to the Atoms-In-Molecules space-partitioning scheme[36] using AIM2000[37] and contact patches according to the non-covalent interactions index NCI[38] were computed using NCI plot (0.1 a.u. grids).[39] The optimized structures (for coordinates see the attached file coordinates.xyz) are shown in Figure S24 and the corresponding computed energies are listed in Table S4.

3. Results and discussion

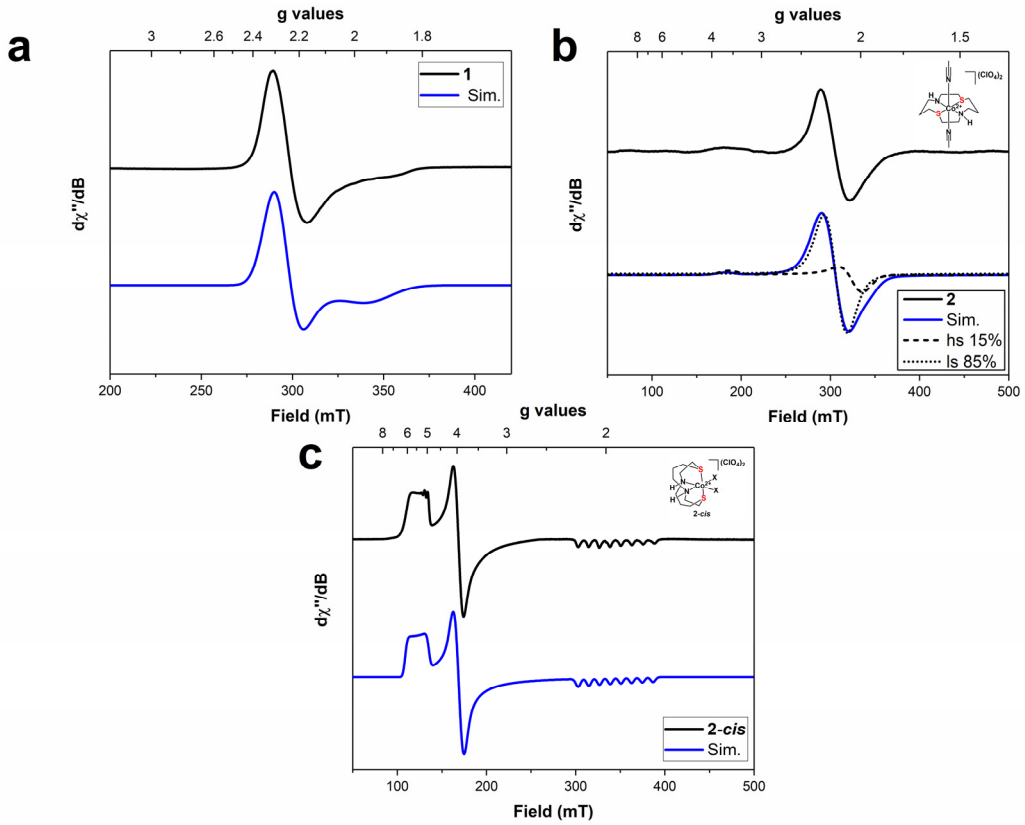

Figure S1. X-band EPR spectra of **1** in MeCN (**a**), **2** in MeCN (**b**) and **2-*cis*** in MeOH ($[Co^{II}(dithiacyclam)(X)_2]^{2+}$) (X = MeOH) (**c**) (black) and corresponding simulated spectra (blue curves). Experimental details: 1 mM complex, ca. 9.35 GHz, 13 K, 1mW power; Simulated parameters: (**a**) $g_{\perp}$=2.27, $g_{\parallel}$=1.94; (**b**) g = 2.19 (85%); $g^{eff}_{\perp}$=3.67, $g^{eff}_{\parallel}$=1.98 (15%); (**c**) g^{eff}_{x} = 5.59, g^{eff}_{y} = 3.77, g^{eff}_{z} = 1.94, A^{eff}_{x} = 9 mT, A^{eff}_{y} = 2.1 mT, A^{eff}_{z} = 11.6 mT.

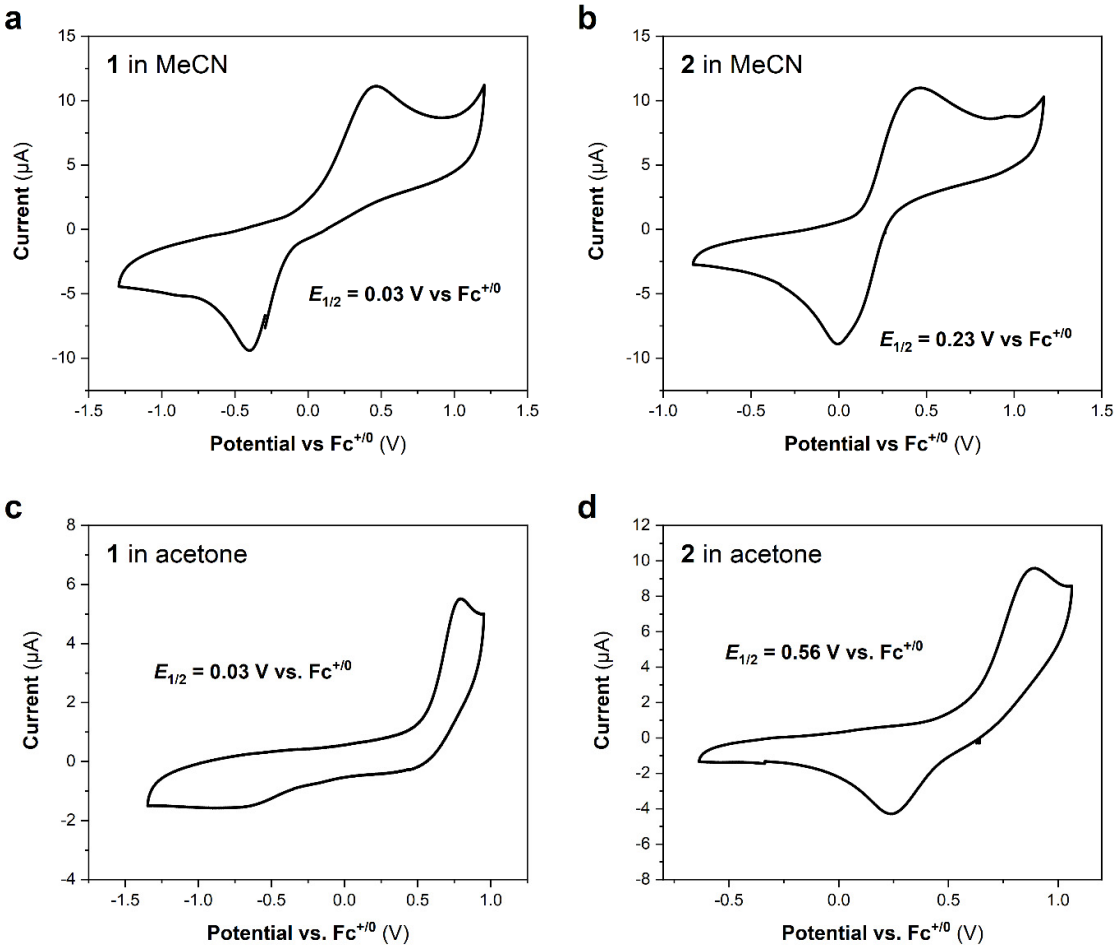

Figure S2. Cyclovoltammograms of **1** and **2** in MeCN (**a**, **b**) and in acetone (**c**, **d**). Experimental details: 1 mM complex, 0.1 M tetrabutylammonium hexafluorophosphate $[(^{n}Bu)_4N]PF_6$, inert atmosphere.

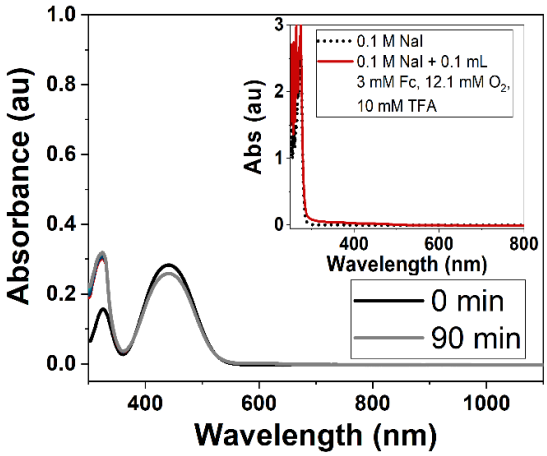

Figure S3. The capability of Fc (3 mM) to reduce O_2 (12.1 mM) in presence of TFA (10 mM) in MeCN at 25 °C was tested in order to subtract the yield in H_2O_2 to that of the two-electron ORR promoted by **1** and **2** under the same reaction conditions (Figure 1 in the main text). By monitoring the reaction for 90 minutes, no formation of Fc^+ (λ_{max} = 619 nm) was detected and iodometric titration (inset) carried out with the use of 0.1 mL of the reaction mixture showed no formation of I_3^- (λ_{max} = 361 nm). This finding proved the lack of H_2O_2 generation in absence of **1** and **2** under the employed conditions.

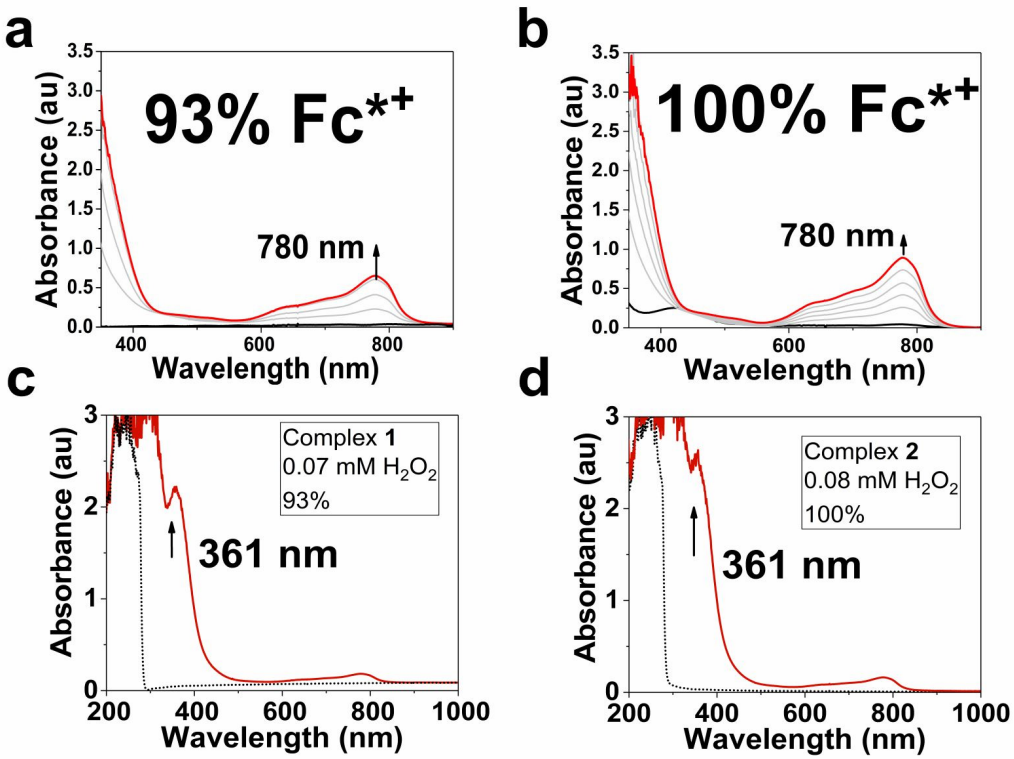

Figure S4. UV-visible spectral changes in the two-electron reduction of O_2 (12.1 mM)[26,40] by Fc* (3 mM) with 0.1 mM **1** (**a**) or **2** (**b**) in presence of 10 mM TFA in O_2-saturated MeCN (2.0 mL total volume) at 25 °C. The absorption spectral changes before (black) and after (red) the addition of 0.1 mL of the reaction mixture of **1**/O_2/Fc* (**c**) or **2**/O_2/Fc* (**d**) in MeCN to an excess of NaI (0.1 M) in MeCN. The percentage yield of Fc^{*+} is based on Fc* and the yield of H_2O_2 is given based on the maximum expected yield of H_2O_2 according to Equation S1 (see below).

$$O_2 + 2Fc^* + 2H^+ = H_2O_2 + 2Fc^{*+} \qquad (S1)$$

$2\ NaI + H_2O_2 \rightarrow I_2 + 2\ NaOH$

$NaI + I_2 \rightarrow NaI_3$

overall: $3\ NaI + H_2O_2 + 2\ H^+ \rightarrow I_3^- + 3\ Na^+ + 2\ H_2O$

Thus $[H_2O_2]_{exp}$ can be determined from the $[I_3^-]$ concentration based on the characteristic absorption @ 361 nm and known $\varepsilon_{361\ nm}$= 28 000 M^{-1} cm^{-1} of I_3^-.

For a 3.0 mM [Fc*] solution maximum concentration of H_2O_2 according to equation 1 is 3.0/2 = 1.5 mM.
Since 0.1 mL of the reaction mixture (total volume = 2.0 mL) is taken for iodometric titration experiments:
Expected maximum $[H_2O_2]$ = (0.1 mL/2.0 mL)·1.5 mM = 0.075 mM

Experimentally determined $[I_3^-] = [H_2O_2]_{exp}$ = 0.07 mM in case of **1** and 0.08 mM in case of **2**, which correspond to 93% and 100%, respectively, of the expected yield of 0.075 mM according to Equation S1.

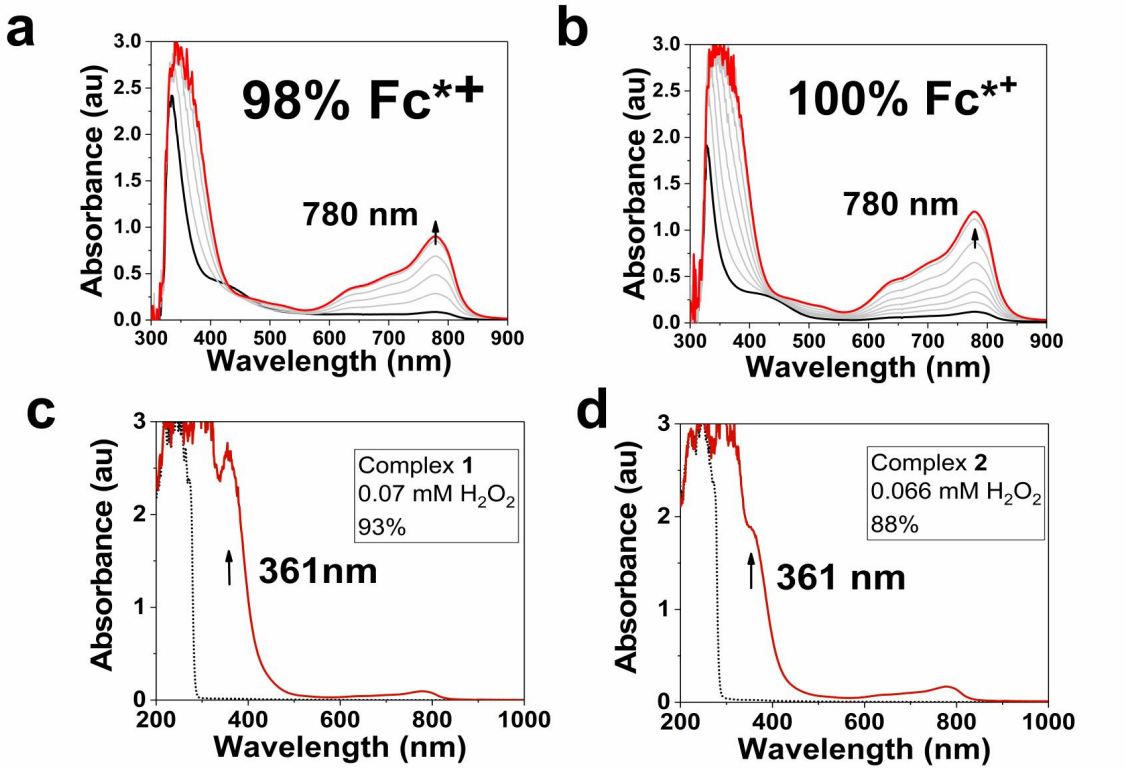

Figure S5. UV-visible spectral changes in the two-electron reduction of O_2 (11.8 mM)[26,40] by Fc* (3 mM) with 0.1 mM **1** (**a**) or **2** (**b**) in presence of 10 mM TFA in O_2-saturated acetone (total volume 2 mL) at 25 °C. The absorption spectral changes before (black) and after (red) the addition of 0.1 mL reaction mixture of **1**/O_2/Fc* (**c**) or **2**/O_2/Fc* in acetone to an excess of NaI (0.1 M) in MeCN under argon atmosphere. The percentage yield of Fc^{*+} is based on Fc* and the yield of H_2O_2 is given based on the maximum expected yield of H_2O_2 according to Equation S1 (see below).

$$O_2 + 2Fc^* + 2H^+ = H_2O_2 + 2Fc^{*+} \qquad (S1)$$

$2\ NaI + H_2O_2 \rightarrow I_2 + 2\ NaOH$

$NaI + I_2 \rightarrow NaI_3$

overall: $3\ NaI + H_2O_2 + 2\ H^+ \rightarrow I_3^- + 3\ Na^+ + 2\ H_2O$

Thus $[H_2O_2]_{exp}$ can be determined from the $[I_3^-]$ concentration based on the characteristic absorption @ 361 nm and known $\varepsilon_{361\ nm}$= 28 000 $M^{-1}\ cm^{-1}$ of I_3^-.

For a 3.0 mM [Fc*] solution maximum concentration of H_2O_2 according to equation 1 is 3.0/2 = 1.5 mM.
Since 0.1 mL of the reaction mixture (total volume = 2.0 mL) is taken for iodometric titration experiments:
Expected maximum $[H_2O_2]$ = (0.1 mL/2.0 mL)·1.5 mM = 0.075 mM

Experimentally determined $[I_3^-] = [H_2O_2]_{exp}$ = 0.07 mM in case of **1** and 0.066 mM in case of **2**, which correspond to 93% and 88%, respectively, of the expected yield of 0.075 mM according to Equation S1.

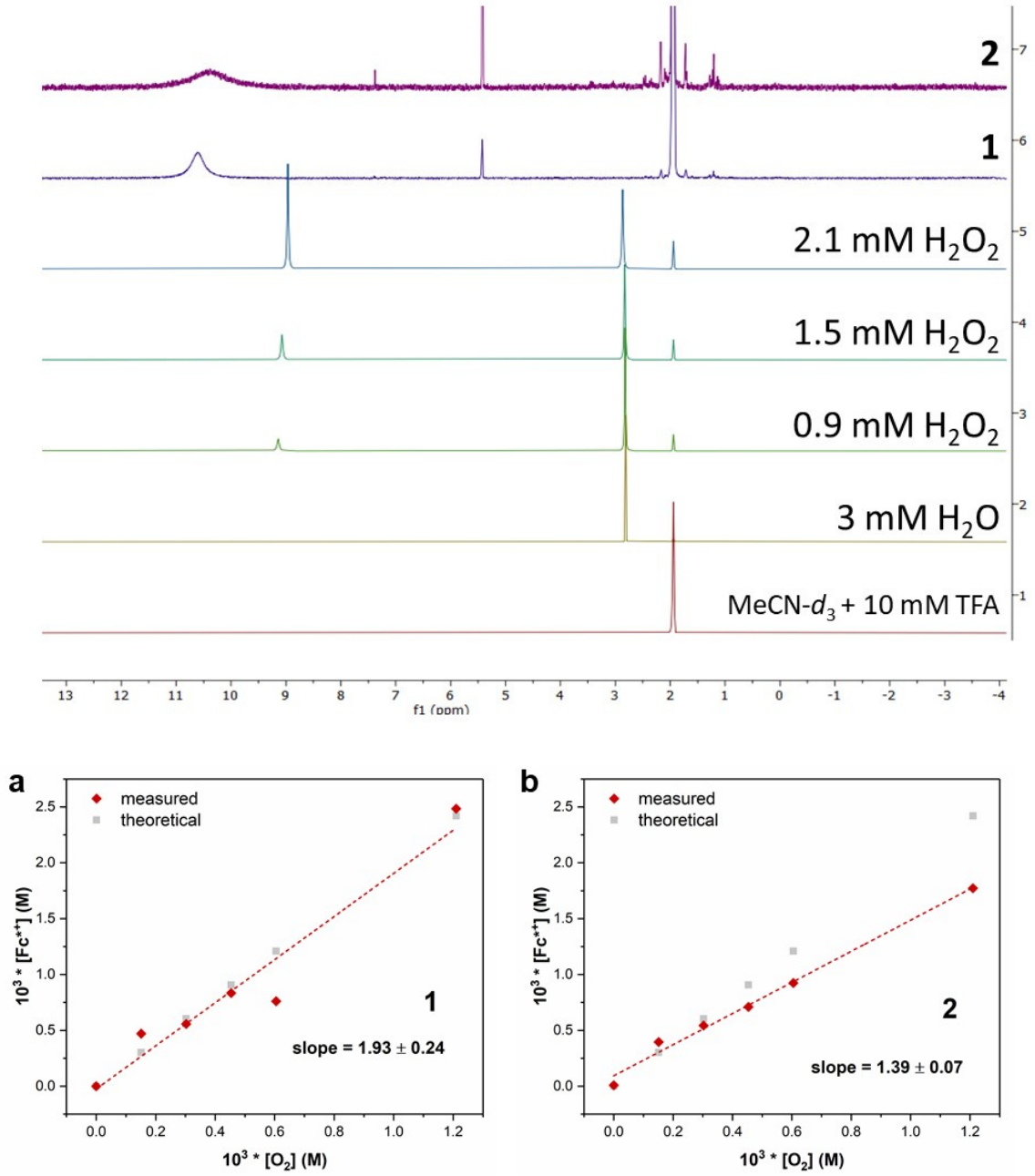

Figure S6. Top: From bottom to top: ^{1}H NMR spectra (300 MHz) of dry and degassed MeCN-d_3 solutions containing a known amount of TFA, H_2O or H_2O_2, showing the peaks of the solvent (1.94 ppm), H_2O (2.81 ppm) and H_2O_2 (expected to be found between 9-11 ppm in a system with a strong hydrogen bonding network).[24] ^{1}H NMR spectra (300 MHz) of the reaction mixture (0.1 mM **1** or **2**, 12.1 mM O_2, 10 mM TFA, 3 mM Fc*, 25 °C, MeCN-d_3/DCM-d_2 9/1) shows peaks at 10.61 ppm for **1** and 10.38 ppm for **2**, corresponding to the predominant formation of H_2O_2 in the catalytic two-electron O_2 reduction performed by **1** and **2**. The peak detected at 5.44 ppm is assigned to dichloromethane-d_2 used to solubilize Fc* in MeCN-d_3. **Bottom**: Plots of the concentration of Fc^{*+} formed in the oxidation of Fc* by dioxygen, catalyzed by **1** (**a**) or **2** (**b**) vs. the concentration of dioxygen (red) and calculated [Fc^{*+}] expected for 2 equiv. Fc* consumption per equiv. of O_2 (grey) (experimental conditions: 3 µM Co, 20 mM TFA, 3.63 mM Fc*, 0.15-1.2 mM O_2, 25 °C, MeCN).

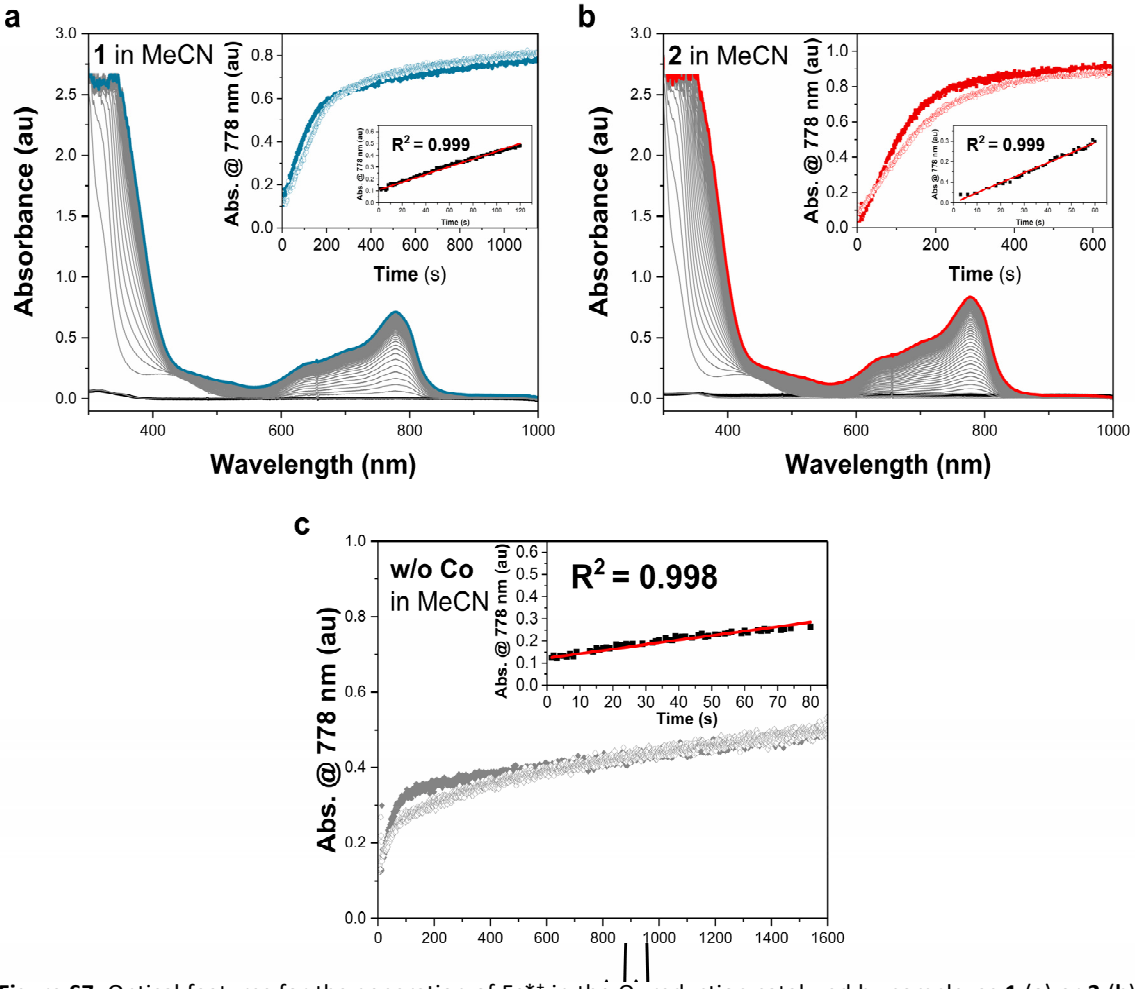

Figure S7. Optical features for the generation of Fc^{*+} in the O_2 reduction catalyzed by complexes **1** (**a**) or **2** (**b**) (10 µM) in MeCN (1 mM Fc*, 10 mM TFA/NaTFA, 0.1 mM urea·H_2O_2,[25] 12.1 mM O_2,[26] 25 °C) and time-course data at λ_{max} = 778 nm[15] with zoom on the linear regression of the initial Fc^{*+} formation rate (inset), that provides the basis for the TOFs associated with the complexes in Table S1. (**c**) Time-course data for the formation of Fc^{*+} (λ_{max} = 778 nm) in absence of Co; inset: the data points are fitted with linear regression to calculate the initial rate of Fc^{*+} formation, which is subtracted from the rate in presence of **1** and **2** to obtain the reported TOFs (see Table S1).

Initial rates of O_2 reduction (M s^{-1}) = (initial rate of [Fc^{*+}]/2)/time

Turnover frequency (TOF) for O_2 reduction (s^{-1}) = initial rate of O_2 reduction/[Co]

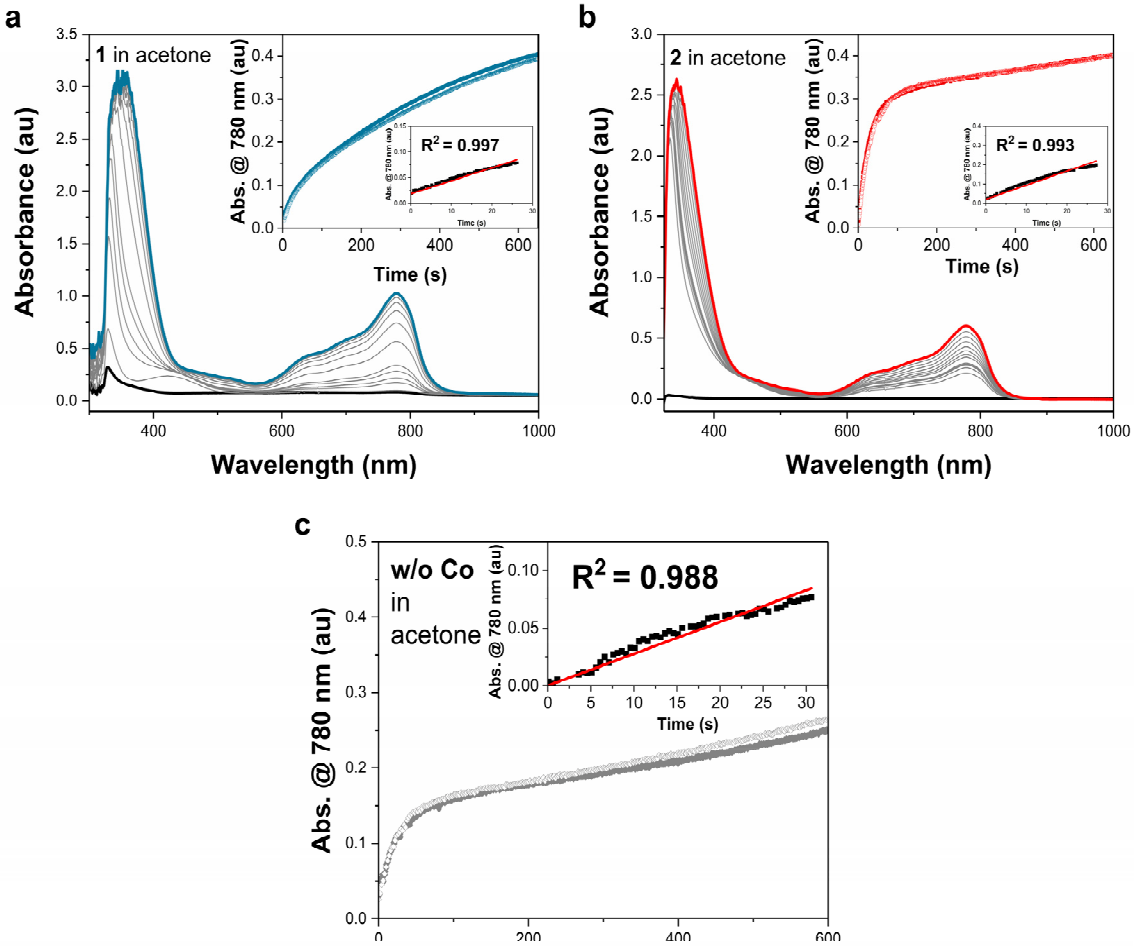

Figure S8. Optical features for the generation of Fc^{*+} in the O_2 reduction catalyzed by complexes **1** (**a**) or **2** (**b**) (10 μM) in acetone (1 mM Fc*, 10 mM TFA/NaTFA, 0.1 mM urea·H_2O_2,[25] 11.8 mM O_2,[40] 25 °C) and time-course data at λ_{max} = 780 nm[14] with zoom on the linear regression of the initial Fc^{*+} formation rate (inset), that provide the basis for the TOFs associated with the complexes in Table S1. (**c**) Time-course data for the formation of Fc^{*+} (λ_{max} = 780 nm) in absence of Co; inset: the data points are fitted with linear regression to calculate the initial rate of Fc^{*+} formation, which is subtracted from the rate in presence of **1** and **2** to obtain the reported TOFs (see Table S1).

Initial rates of O_2 reduction (M s^{-1}) = (initial rate of [Fc^{*+}]/2)/time

Turnover frequency (TOF) for O_2 reduction (s^{-1}) = initial rate of O_2 reduction/[Co]

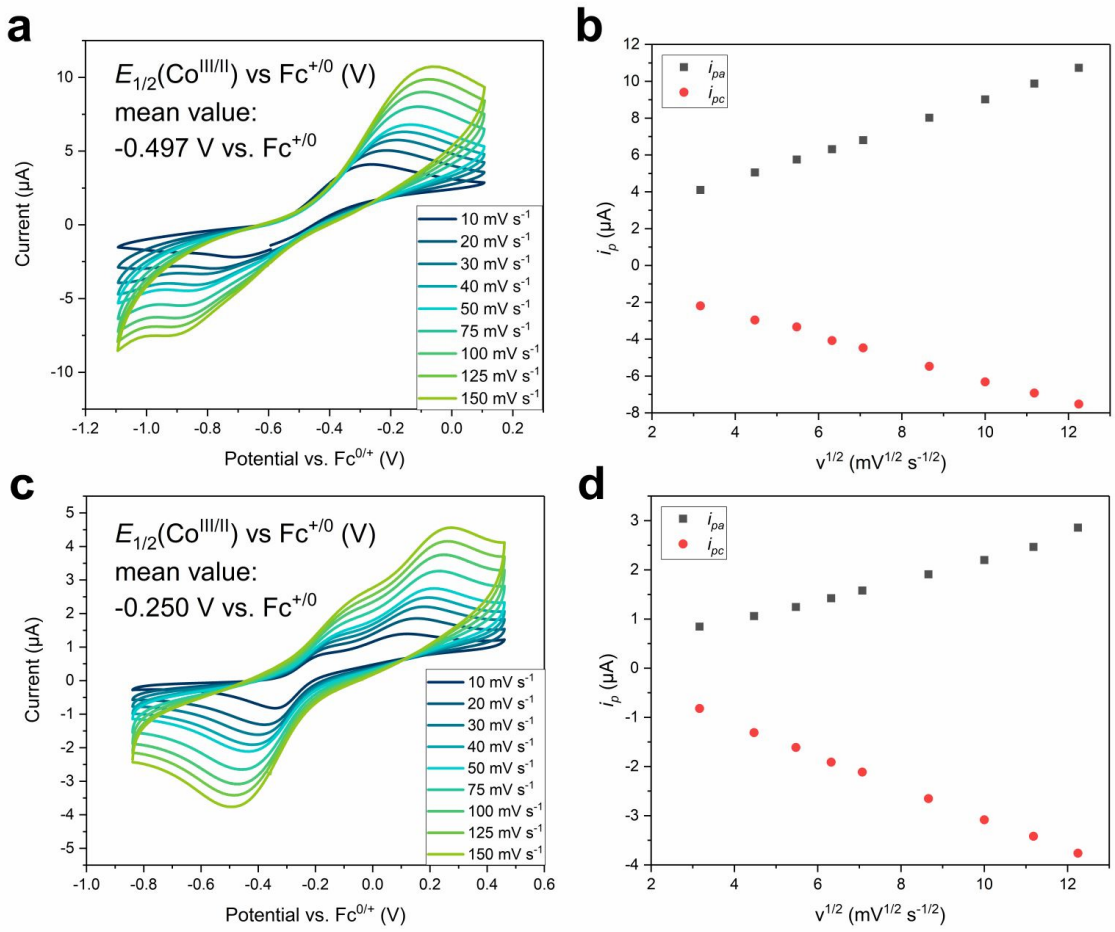

Figure S9. Cyclovoltammetric analysis of **1** (**a**) and **2** (**c**) (1 mM) in MeCN, in presence of TFA and NaTFA (10 mM each, *buffered* conditions) recorded at different scan rate. Supporting electrolyte: 0.1 M $[(^nBu)_4N]PF_6$. Linear dependence of the peak current versus the square root of the scan rate showed reversible behavior for the redox couple $Co^{III/II}$ in both **1** (**c**) and **2** (**d**), allowing $E_{1/2}(Co^{III/II})$ assignments, used for the effective overpotential determination (Table S1, Scheme S1).

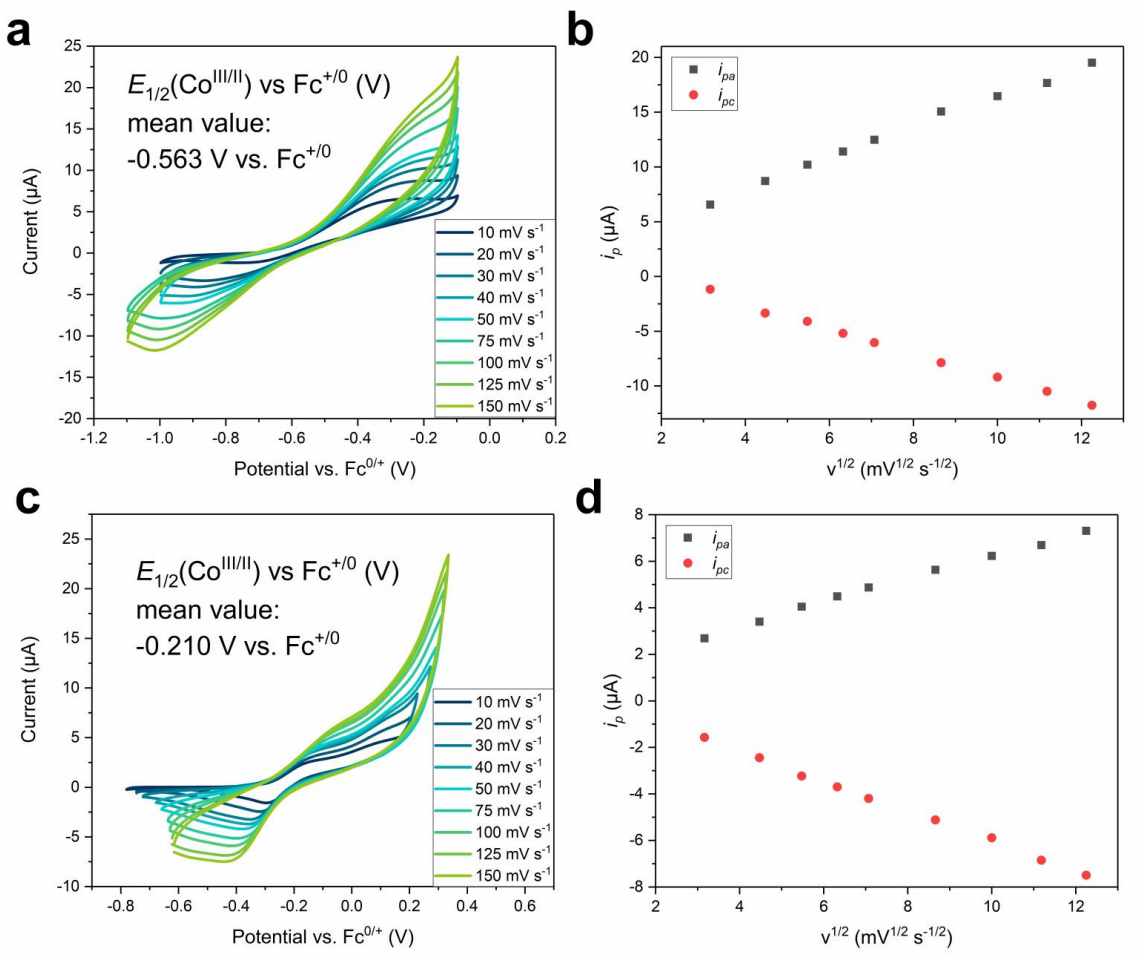

Figure S10. Cyclovoltammetric analysis of **1** (**a**) and **2** (**c**) (1 mM) in acetone, in presence of TFA and NaTFA (10 mM each, *buffered* conditions) recorded at different scan rate. Supporting electrolyte: 0.1 M $[(^nBu)_4N]PF_6$. Linear dependence of the peak current versus the square root of the scan rate shows reversible behavior for the redox couple $Co^{III/II}$ in both **1** (**c**) and **2** (**d**), allowing $E_{1/2}(Co^{III/II})$ assignments, used for the effective overpotential determination (Table S1, Scheme S1).

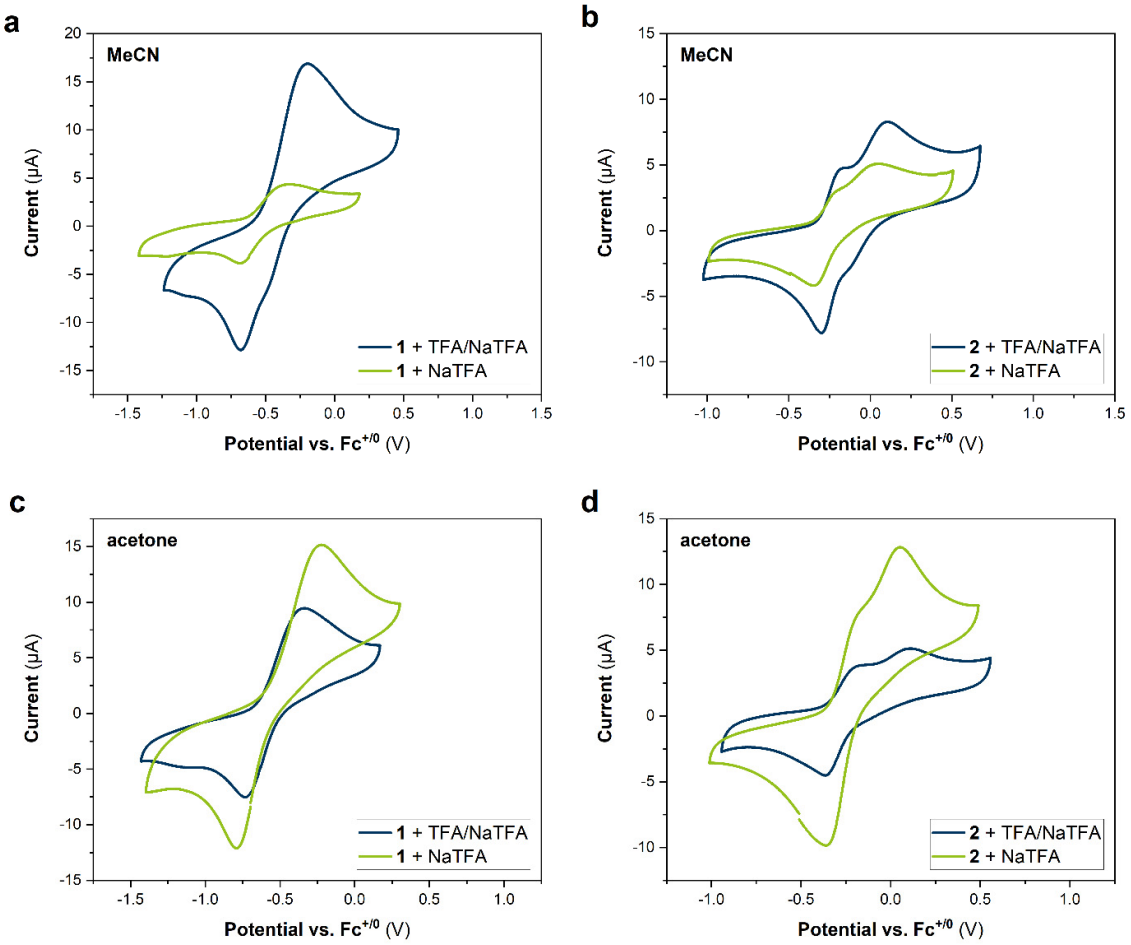

Figure S11. Comparison between the CVs of **1** and **2** (1 mM) in presence of 10 mM NaTFA (green) and of **1** and **2** (1 mM) in presence of 10 mM TFA/NaTFA (blue) in MeCN (**a** and **b**) and acetone (**c** and **d**). Supporting electrolyte: 0.1 M $[(^{n}Bu)_4N]PF_6$.

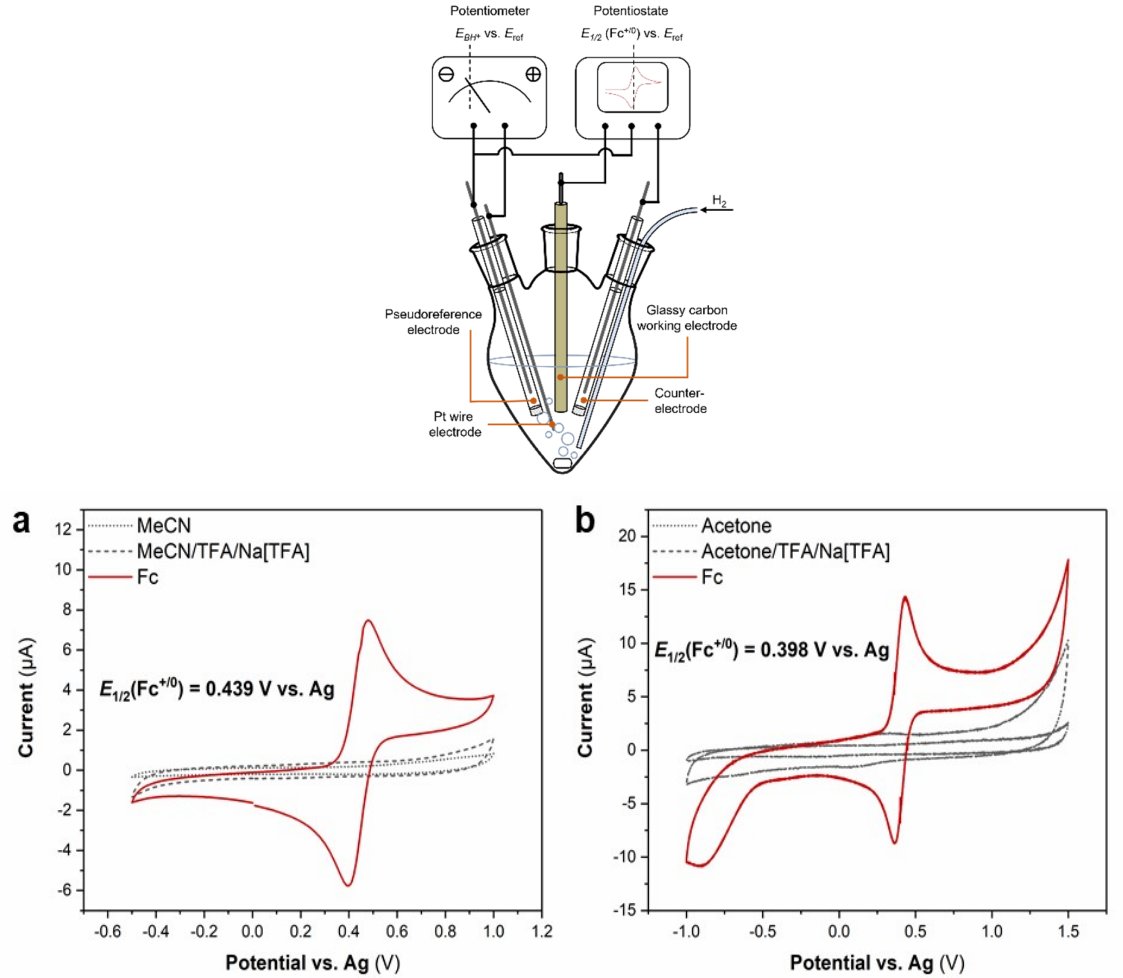

Figure S12. Top: Schematic representation of the cell configuration used for the open-circuit potential (OCP) measurements in organic media.[27] **Bottom:** Cyclic voltammograms of the reference compound (Fc) in organic media under different reaction conditions: (**a**) 10 mM TFA and NaTFA in MeCN; (**b**) 10 mM TFA and NaTFA in acetone. Supporting electrolyte: 0.1 M $[(^nBu)_4N]PF_6$.

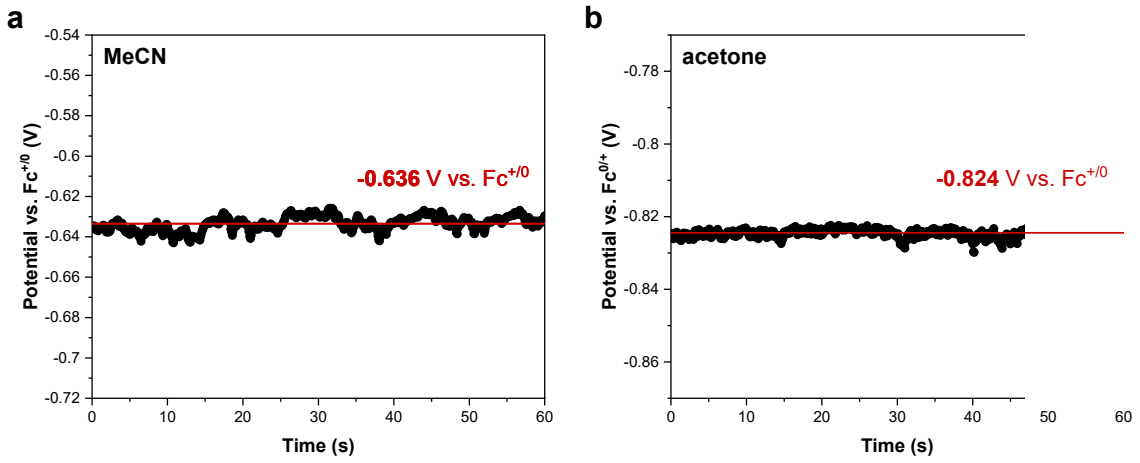

Figure S13. OCP measurements of $E_{H+/H2}$ under 1 atm H_2 with different reaction conditions: (**a**) 10 mM TFA and NaTFA in MeCN; (**b**) 10 mM TFA and NaTFA in acetone. Supporting electrolyte: 0.1 M $[(^nBu)_4N]PF_6$.

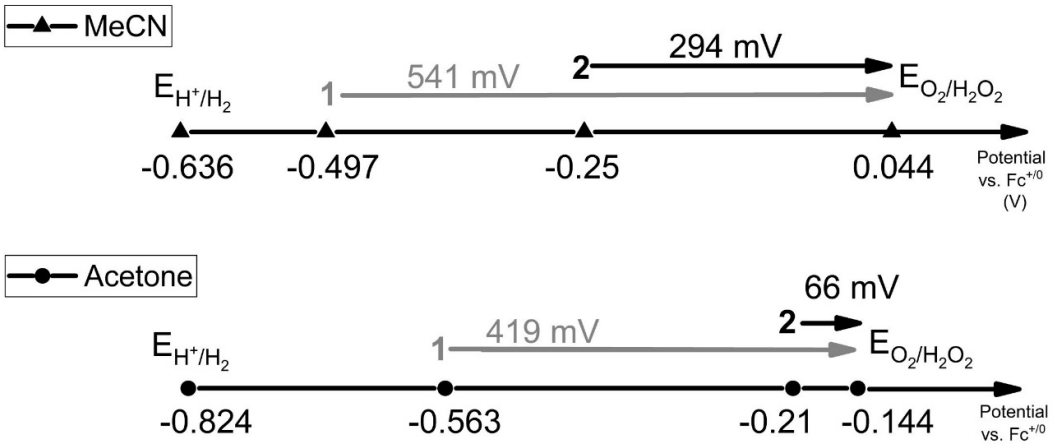

Scheme S1. Redox potential scale showing $E_{1/2}(Co^{III/II})$ for **1** and **2** and thermodynamic reduction potentials for H^+/H_2 and O_2/H_2O_2 in V vs. $Fc^{+/0}$ in organic media (MeCN and acetone).

Table S1. TOFs for two-electron dioxygen reduction catalyzed by **1** and **2**, $E_{1/2}(Co^{III/II})$ and η_{eff} for **1** and **2** under buffered conditions in different solvation environments, compared with the corresponding values reported for one of the best cobalt non-heme two-electron dioxygen reduction catalyst **CoN_2O_2**.[41]

TOF (s^{-1})	**1**	**2**	**CoN_2O_2**[41]
MeCN	0.124	0.250	
Acetone	0.131	0.298	
MeOH			0.027
$E_{1/2}(Co^{III/II})$ (V vs. $Fc^{+/0}$)	**1**	**2**	**CoN_2O_2**[41]
MeCN	-0.497	-0.250	
Acetone	-0.563	-0.210	
MeOH			-0.280
η_{eff} (V)	**1**	**2**	**CoN_2O_2**[41]
MeCN	0.541	0.294	
Acetone	0.419	0.066	
MeOH			0.150

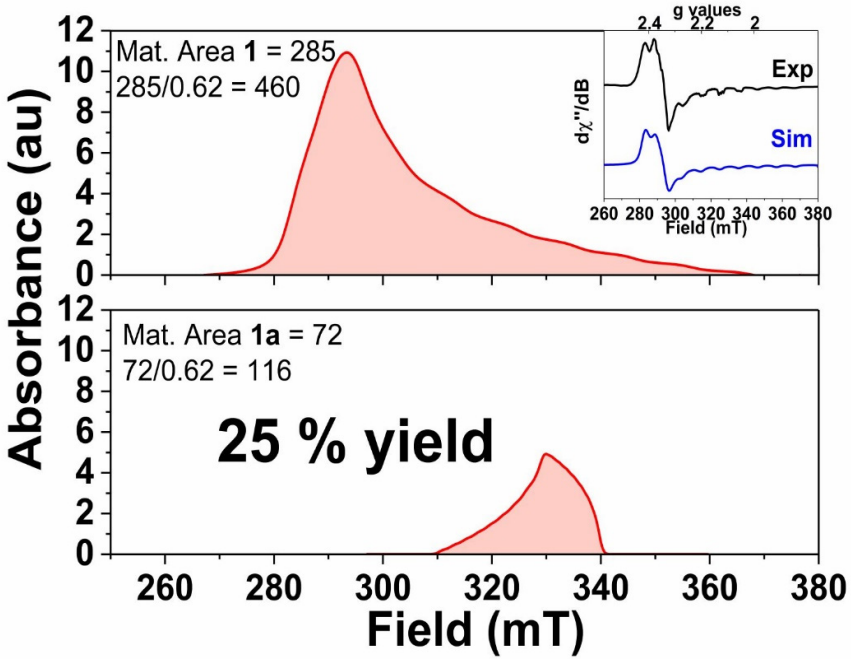

Figure S14. Comparison of the integrated areas of the X-band EPR spectrum of **1** (shown in the inset. Simulated parameters: g_x = 2.29, g_y = 2.26, g_z = 2.02; A_x = 1 mT, A_y = 0 mT, A_z = 10.7 mT) and **1a** (Figure 2b) in acetone displayed a yield of 25 % **1a**, referring to the initial Co(II) concentration.

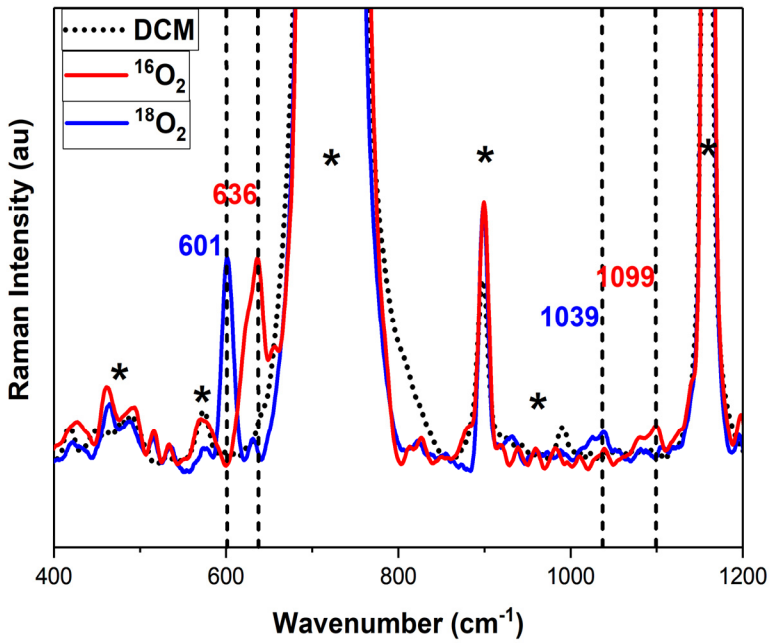

Figure S15. rR spectrum of **1** (8 mM) in methylene chloride (DCM) after O_2 exposure at –70 °C, obtained with 406 nm excitation, shows vibrational mode attributable to **1a** ($\nu_{16O\text{-}16O}$ = 1099 cm^{-1}) and **1b** ($\nu_{Co\text{-}16O}$ = 636 cm^{-1}).

Table S2. Complete list of DFT calculated Co–O, O–O and S-O-O-Co vibrations for **1a**/**1b** and **2a**/**2b** (where IR and rR indicates the computed vibration intensity) in comparison with the experimentally observed.

* Given bond distances are the O–O bond distances.

model	**dft-1a: 1.330 Å* (fix)**									**Experimentally observed**
	^{16}O-^{16}O			**^{18}O-^{18}O**						
band	cm^{-1}	IR	Raman	cm^{-1}	IR	Raman				$^{16}O_2$($^{18}O_2$) (cm^{-1})
Co-O	595	2	16	570	2	8				
H···O-O	**1078**	82	72	**1033**	89	120				**1099(1039)**
O-O sym	1110	68	48	1095	100	2				
model	**dft-1b (^{16}O-^{16}O) 1.449 Å* (opt)**			**dft-1b (^{16}O-^{16}O) 1.507 Å* (fix)**			**dft-1b (^{18}O-^{18}O) 1.507 Å (fix)**			
band	cm^{-1}	IR	Raman	cm^{-1}	IR	Raman	cm^{-1}	IR	Raman	
Co-O sym	566	80	1	562	168	0	530	67	0	**641(610)**
Co-O asym	673	0	57	**674**	0	43	**640**	0	42	**757(727)**
O-O stretch	907	0	100	**765**	0	33	**722**	0	29	
model	**dft-2a: 1.449 Å* (opt)**									**795(764)** (observed for $^{16,18}O_2$ = **795 sh, 764, 745 sh, 725 sh**)
	^{16}O-^{16}O-(S)			**^{16}O-^{18}O-(S)**						
band	cm^{-1}	IR	Raman	cm^{-1}	IR	Raman				
Co-O	466	20	20	465	21	20				
Co-O asym	776	39	21							
O-O asym	**789**	11	20	**758**	50	30				
O-O sym	837	13	10	805	5	26				
model	**^{18}O-^{16}O-(S)**			**^{18}O-^{18}O-(S)**						
band	cm^{-1}	IR	Raman	cm^{-1}	IR	Raman				
Co-O	455	15	19	454	15	19				
O-O asym	**768**	37	41	**747**	39	42				
O-O sym	816	7	19	796	10	9				
model	**dft-2b (^{16}O-^{16}O) 1.429 Å* (opt)**			**dft-2b (^{16}O-^{16}O) 1.500 Å (fix)**			**dft-2b (^{18}O-^{18}O) 1.500 Å (fix)**			
band	cm^{-1}	IR	Raman	cm^{-1}	IR	Raman	cm^{-1}	IR	Raman	
Co-O sym	558	217	2	559	246	3	538	186	2	
Co-O asym	665	2	60	673	2	57	639	2	49	
O-O stretch	920	1	476	**760**	0	110	**717**	0	98	**764(725)**

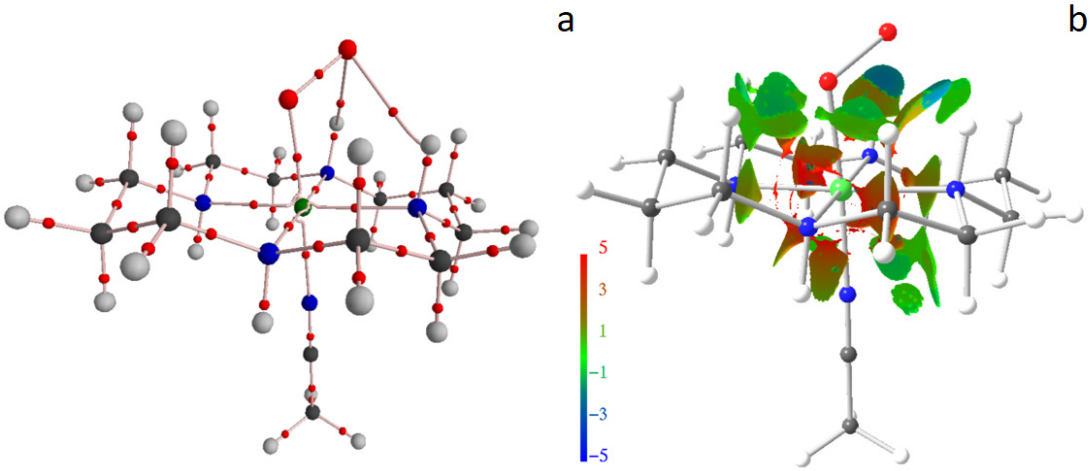

Figure S16. AIM bond topology (**a**) and NCI contact patches (**b**) revealing the special role of intramolecular N–H···O interactions in stabilizing the Co–superoxo moiety **1a**.

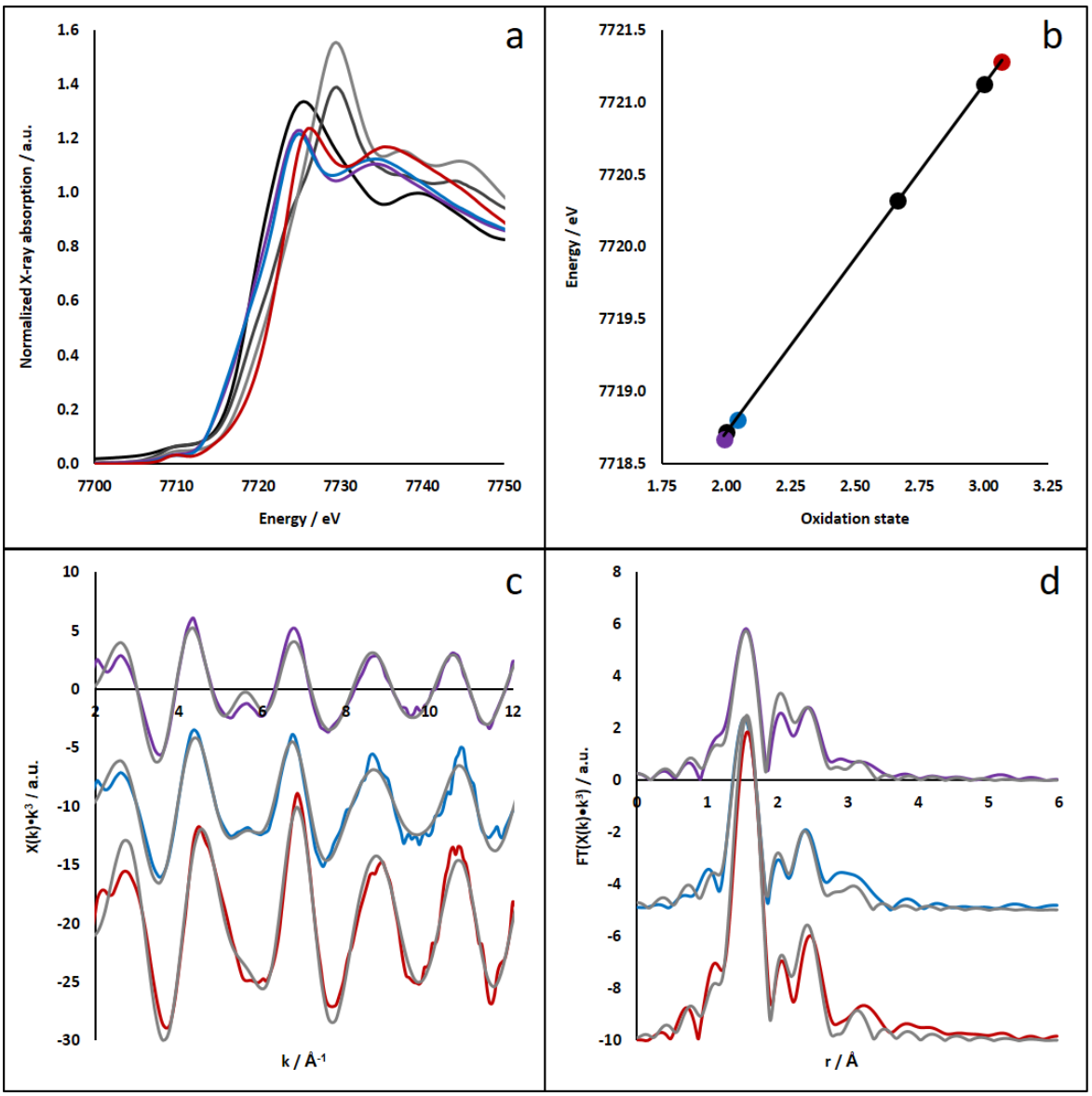

Figure S17. Co K-edge XAS spectra of **1**-solid (purple), **1**-solution (blue), and **1a**/**1b** (red). (**a**) XANES of **1** including $Co(H_2O)_6(NO_3)_2$ (black), Co_3O_4 (dark grey), and CoOOH (light grey) as reference compounds. (**b**) Oxidation states determined by the integral method: 2.0 (**1**-powder), 2.0 (**1**-solution), and 3.1 (**1a**/**1b**). (**c**) k-space EXAFS spectra (k^3 weighted) and respective fits (grey lines). (**d**) Fourier transform of the EXAFS spectra.

Table S3. EXAFS Least Squares fitting results for **1, 1a**/**1b** and **2**, **2a**/**2b**.

model	shell	N	err	R	err	σ	err	shell	N	err	R	err	σ	err
1-solid								Co-N	4		1.98	0.01	0.058	0.011
1-solution								Co-N	4		1.95	0.01	0.037	0.013
1-O$_2$	Co-O	1		1.86	0.02	0.032		Co-N	5		1.96	0.01	0.032	
model	**shell**	**N**	**err**	**R**	**err**	**σ**	**err**	**shell**	**N**	**err**	**R**	**err**	**σ**	**err**
1-solid	Co-N	2		2.24	0.03	0.058								
1-solution	Co-N	1		2.12	0.05	0.037		Co-N	1		2.52	0.06	0.037	
1-O$_2$														
model	**shell**	**N**	**err**	**R**	**err**	**σ**	**err**	**shell**	**N**	**err**	**R**	**err**	**σ**	**err**
1-solid	Co-C	4		2.81	0.04	0.058		Co-C	4		2.96	0.05	0.058	
1-solution	Co-C	4		2.77	0.04	0.037		Co-C	4		2.92	0.04	0.037	
1-O$_2$	Co-C	4		2.80	0.02	0.032		Co-C	4		2.93	0.02	0.032	
model	**shell**	**N**	**err**	**R**	**err**	**σ**	**err**	**Rf**						
1-solid	Co-C	2		3.43	0.09	0.058		**17.5**						
1-solution	Co-C	2		3.39	0.07	0.037		**14.3**						
1-O$_2$	Co-C	2		3.36	0.05	0.032		**14.7**						

model	shell	N	err	R	err	σ	err	shell	N	err	R	err	σ	err
2-solid								Co-N	2		2.02	0.02	0.041	0.024
2-solution								Co-N	2		2.02	0.02	0.041	0.026
2-O$_2$	Co-O	0.8	0.5	1.83	0.07	0.057	0.035	Co-N	3		2.03	0.04	0.057	
model	**shell**	**N**	**err**	**R**	**err**	**σ**	**err**	**shell**	**N**	**err**	**R**	**err**	**σ**	**err**
2-solid	Co-N	2		2.32	0.04	0.041		Co-S	2		2.26	0.01	0.041	
2-solution	Co-N	2		2.11	0.04	0.041		Co-S	*0.7*	*0.1*	2.28	0.07	0.041	
2-O$_2$	Co-N	1		2.33	0.24	0.057		Co-S	*1.1*	*0.4*	2.27	0.08	0.057	
model	**shell**	**N**	**err**	**R**	**err**	**σ**	**err**	**shell**	**N**	**Err**	**R**	**err**	**σ**	**err**
2-solid														
2-solution	Co-S	*0.7*	*0.1*	2.46	0.06	0.041		Co-S	*0.7*	*0.1*	3.37	0.05	0.041	
2-O$_2$	Co-S	*0.5*	*0.4*	2.44	0.13	0.057		Co-S	*0.5*	*0.4*	3.42	0.29	0.057	
model	**shell**	**N**	**err**	**R**	**err**	**σ**	**err**	**shell**	**N**	**err**	**R**	**err**	**σ**	**err**
2-solid	Co-C	4		2.98	0.03	0.041		Co-C	2		3.10	0.06	0.041	
2-solution	Co-C	4		3.02	0.02	0.041								
2-O$_2$	Co-C	2		2.96	0.06	0.057								
model	**shell**	**N**	**err**	**R**	**err**	**σ**	**err**	**Rf**						
2-solid	Co-C	4		3.52	0.03	0.041		**8.8**						
2-solution	Co-C	6		3.49	0.02	0.041		**12.6**						
2-O$_2$	Co-C	6		3.50	0.07	0.057		**13.6**						

Populations (N) without error are fixed; N for Co-S shells in **2** displayed in *italic* are restrained to a summed-up value of 2. Due to Co-N- and Co-C-shells overlapping with Co-S shells at about 2.2-2.3 and 3.3-3.5 Å, the populations of the former, N(N) and N(C), were held fixed in the fits.

Table S4. Top: Comparison between Co coordination sphere obtained by EXAFS and respective DFT-models. **Bottom:** Energy comparison between DFT-computed structures; coordinates are provided for the models highlighted in green (see Figure S24 for the optimized molecular structures).

	1-solid		**dft-1**	
	N	R	n	d
Co-N	4	1.98	4	2.00
Co-N	2	2.24	2	2.24
	1-solution		**dft-1'**	
	N	R	n	d
Co-N	4	1.95	4	1.99
Co-N	1	2.12	1	2.10
Co-N	1	2.52		

	1a/1b		**dft-1a**		**dft-1b**	
	N	R	n	d	n	d
Co-O	1	1.86	1	1.86	1	1.87
Co-N	5	1.96	1	1.93	1	1.91
Co-N			4	1.98	4	1.98

	2-solid		**dft-2**	
	N	R	n	d
Co-N	2	2.02	2	2.02
Co-N	2	2.32	2	2.22
Co-S	2	2.26	2	2.25
	2-solution			
	N	R		
Co-N	2	2.02		
Co-N	2	2.11		
Co-S	0.7(1)	2.28		
Co-S	0.7(1)	2.46		
Co-S	0.7(1)	3.37		

	2a/2b		**dft-2a**		**dft-2b**	
	N	R	n	d	n	d
Co-O	0.8(5)	1.83	1	1.94	1	1.86
Co-N	2	2.02	1	2.06	1	1.91
Co-N	2	2.11	1	2.12	2	1.99
Co-N			1	2.17		
Co-S	1.1(4)	2.27			2	2.24
Co-S	0.5(4)	2.44	1	2.36		
Co-S	0.5(4)	3.42	1	3.21		

Optimized structure	**S**	**E** **a.u.**	**ΔE** **a.u.**	**kJ/mol**	**status**	**note**
1	**1/2**	-2262.6575			optimized	
1	**3/2**	-2262.6456	0.0120	31.5	optimized	
1	**5/2**				not conducted	
1'	**1/2**	-2129.8832			optimized	
1'	**3/2**	-2129.8679	0.0153	40.1	optimized	
1'	**5/2**				not conducted	
1a	**1/2**	-2280.2172			optimized; O-O=1.330Å	
1a	**3/2**				unstable	
1a	**5/2**				not conducted	
1b	**0**	-4410.1361			optimized; O-O=1.507Å	

Optimized structure		E a.u.	ΔE a.u.	ΔE kJ/mol	status	note
2	**1/2**	-2948.2927			optimized	
2	**3/2**	-2948.2779	0.0148	39.0	optimized	
2	**5/2**				not conducted	
2a-trans	**1/2**	-2965.7926			optimized	
2a-trans	**3/2**	-2965.7862	0.0064	16.9	optimized	ΔE = **2a-*trans***(S=3/2) – **2a-*trans***(S=1/2)
2a-trans	**5/2**	-2965.7752	0.0175	45.9	optimized	ΔE = **2a-*trans***(S=5/2) – **2a-*trans***(S=3/2)
				62.8		ΔE = **2a-*trans***(S=5/2) – **2a-*trans***(S=1/2)
2a-cis	**1/2**				unstable	
2a-cis	**3/2**	-2965.7874	-0.0012	-3.0	optimized	ΔE = **2a-*cis***(S=3/2) – **2a-*trans***(S=3/2)
2a-cis	**5/2**	-2965.7549	0.0325	85.2	optimized	ΔE = **2a-*cis***(S=5/2) – **2a-*cis***(S=3/2)
2b	**0**	-5781.3982			optimized; O-O=1.500A	

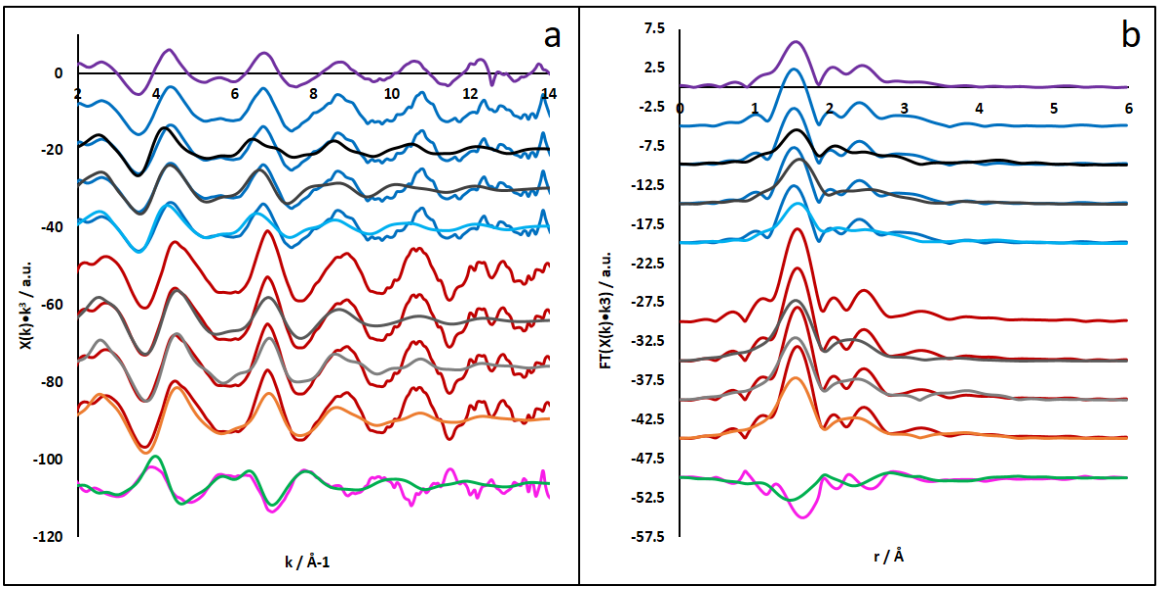

Figure S18. Experimental and simulated EXAFS spectra (**a**) and FT of EXAFS (**b**) for **1**, **1a**, and **1b**. Color-code: purple = experimental **1**-solid; blue = experimental **1**-solution; black = **dft-1**, dark grey = **dft-1'**; light blue = the best fit for EXAFS and FT corresponding to the superposition of **dft-1** (50%) and **dft-1'** (50%); red = experimental **1a**/**1b**; medium grey = **dft-1a**, light grey = **dft-1b**, orange = the best fit for EXAFS and FT corresponding to the superposition of **dft-1a** (50%) and **dft-1b** (50%). The validity of the fit is further corroborated by the reasonable match of the difference spectra of experimental **1-1a**/**1b** (pink trace) with that of the difference spectra (green trace) of **dft-1/dft-1'** (light blue) and **dft-1a/dft-1b** (orange) spectra. For the DFT calculated structures see Figure S24a-d.

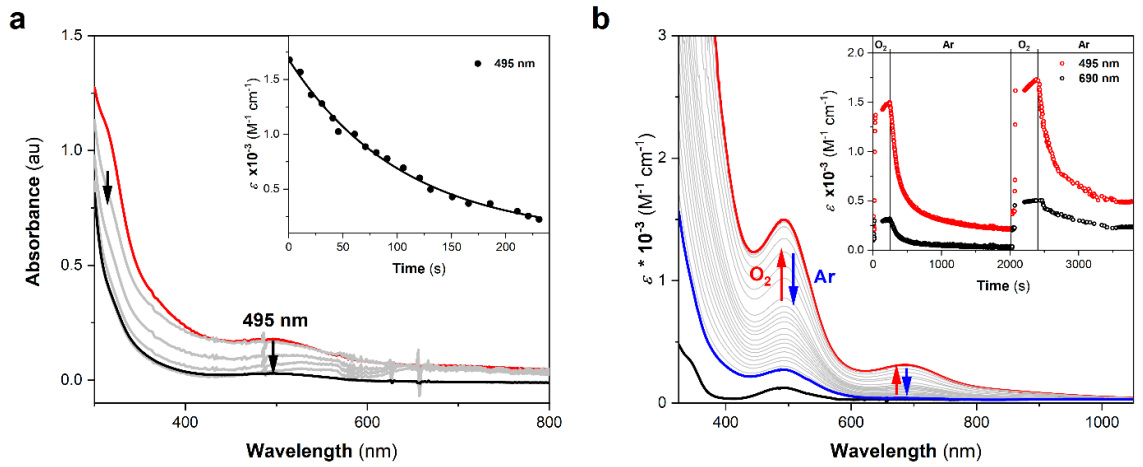

Figure S19. (**a**) Decay of the optical features of a MeCN solution of **2a**/**2b** (red) at 25 °C (inset: time trace at λ_{max} = 495 nm). (**b**) Generation of **2a**/**2b** (red) after O_2 bubbling in a 1 mM MeCN solution of **2** (black) at –30 °C and decay after Ar flushing (blue). The time trace in the inset shows the re-generation of **2a**/**2b** after oxygenation of the same solution.

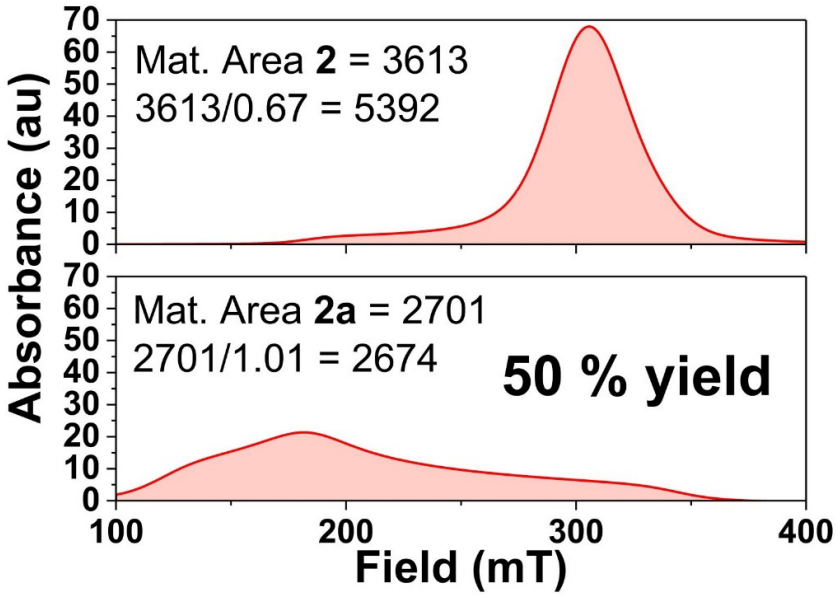

Figure S20. Double integration of the simulated X-band EPR spectra of 1 mM MeCN solution of **2** (Figure S1b) (top) and **2a** (bottom) generated by O_2 exposure at –30 °C of the same solution of **2** (no change in Co concentration); comparison of the integrated areas shows a yield of 50 % **2a**, referring to the initial Co(II) concentration.

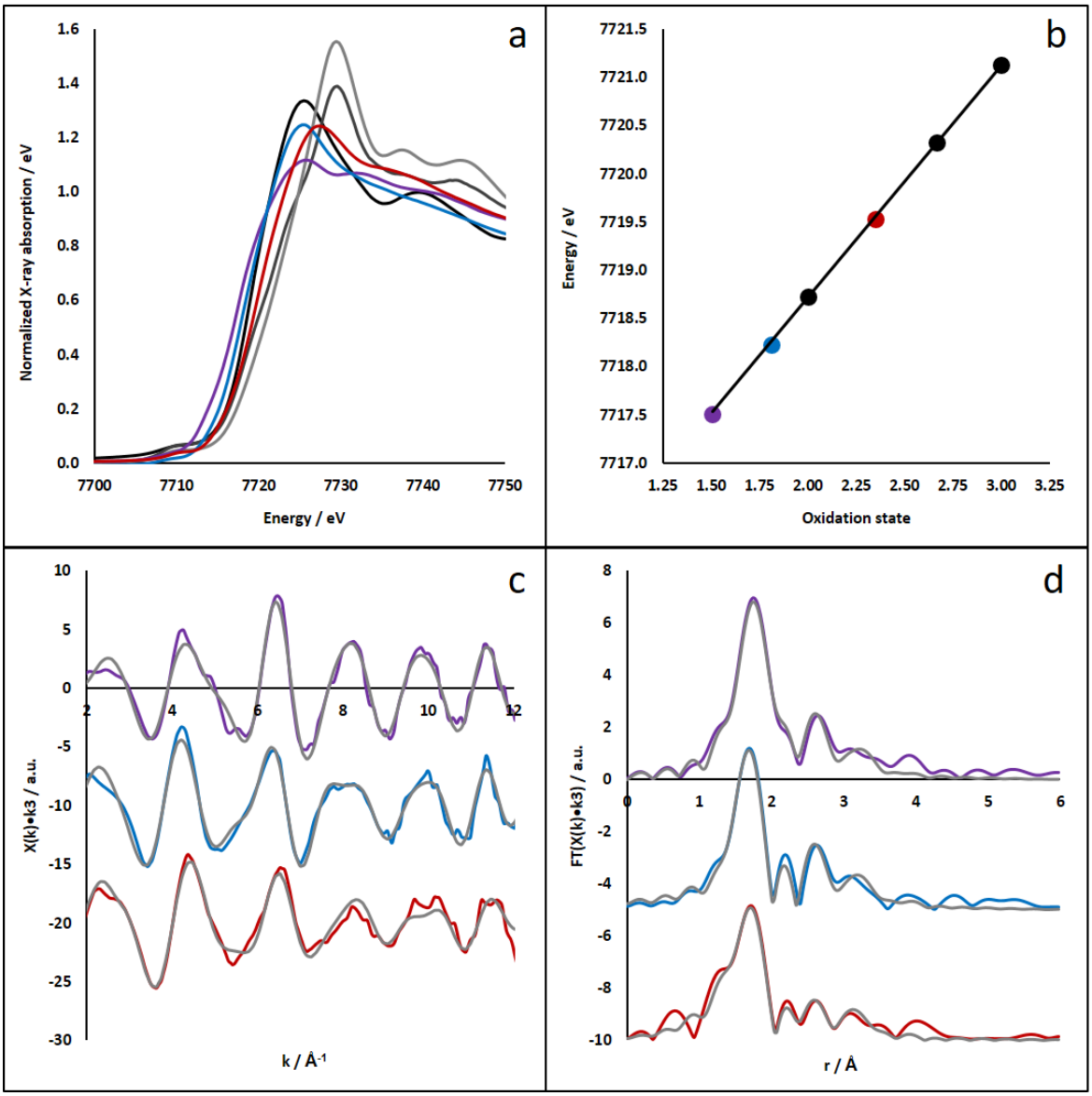

Figure S21. Co K-edge XAS spectra of **2**-powder (purple), **2**-solution (blue), and **2a**/**2b** (red). (**a**) XANES of **2** including $Co(H_2O)_6(NO_3)_2$ (black), Co_3O_4 (dark grey), and CoOOH (light grey) as reference compounds. (**b**) Oxidation states determined by the integral method: 1.5 (**2**-powder), 1.8 (**2**-solution), and 2.4 (**2a**/**2b**). (**c**) k-space EXAFS spectra (k^3 weighted) and respective fits (grey lines). (**d**) Fourier transform of the EXAFS spectra.

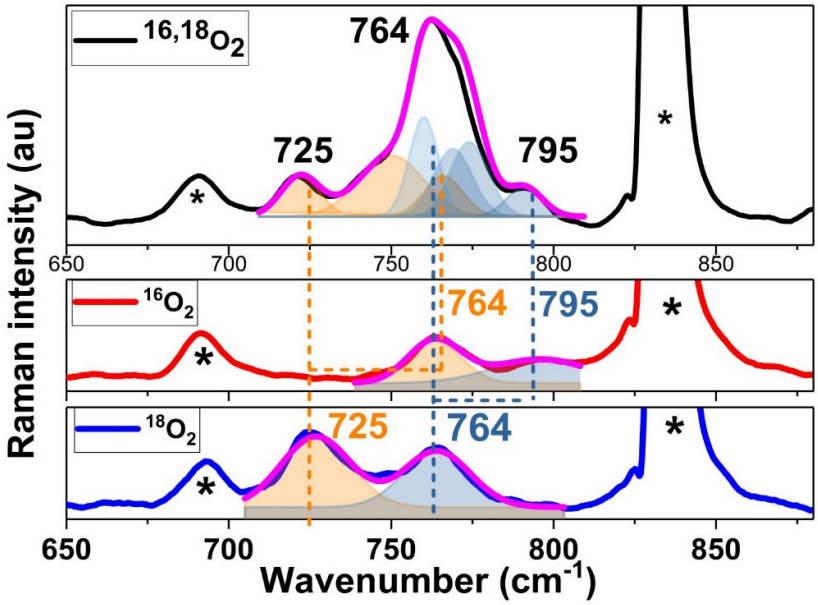

Figure S22. rR spectra of **2a**/**2b** (8 mM) in MeCN-d_3 solution at –30 °C generated by 514 nm excitation, where **2a**/**2b** were obtained from **2** with the use of a 1:2:1 mixture of ^{16}O-^{16}O/^{16}O-^{18}O/^{18}O-^{18}O (black) $^{16}O_2$ (red) or $^{18}O_2$ (blue). When spectra deconvolution was performed by employing the DFT-computed vibrations for the dimeric Co(III)–peroxo species **2b** (orange) and the monomeric Co(III)–peroxo species **2a** (light blue) (Table S2), the overall curve (pink) could well resemble the observed experimental features.

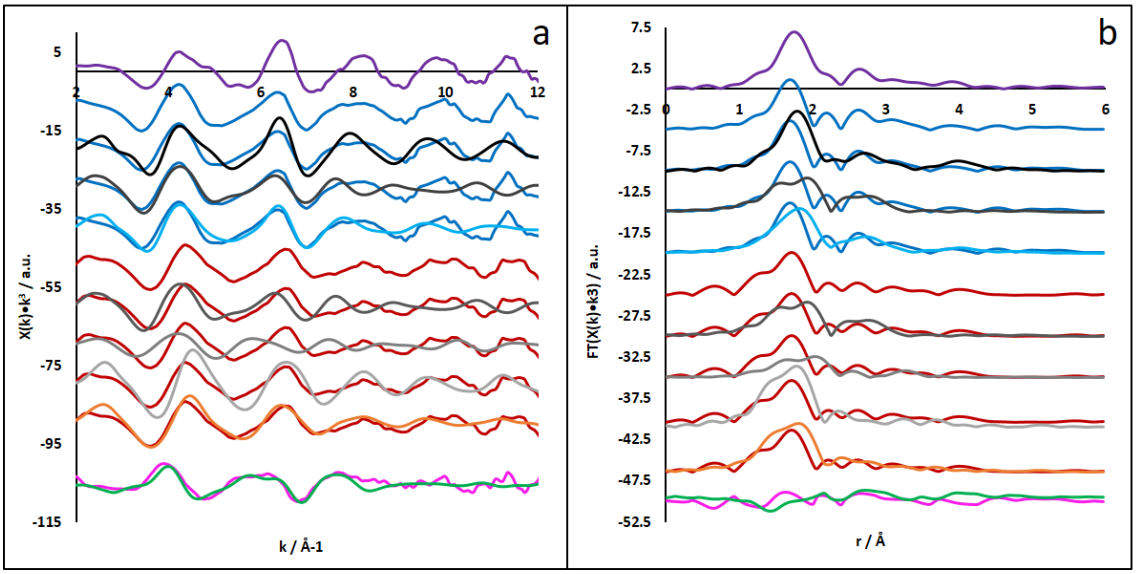

Figure S23. Experimental and simulated EXAFS spectra (**a**) and FT of EXAFS (**b**) for **2**, and **2a**/**2b**. Color-code: purple = experimental spectrum for **2**-solid, blue = experimental spectrum for **2**-solution; black = **dft-2**, which can nicely reproduce the experimental feature in **2**-solid; The best fit of **2**-solution, however, corresponds to superposition of **dft-2** (50%) and **dft-2a** (trans-isomer 50%), thereby suggesting partially oxidation in solution; red = experimental spectra for an O_2 saturated solution of **2**; dark grey = **dft-2a** (*trans*-isomer); medium grey = **dft-2a** (*cis* isomer), whose formation can be clearly excluded based on the calculated EXAFS and FT features; light grey = calculated spectra of the dimer, **dft-2b**; orange = The best fit that can reproduce the experimental spectra (blue trace) corresponds to the superposition of **dft-2a** (*trans*-isomer) (50%) and **dft-2b** (50%). The validity of the fit is further corroborated by the reasonable match of the difference spectra of experimental **2-2a**/**2b** (pink trace) with that of the difference spectra (green trace) of superpositions (blue trace-orange trace). For the DFT calculated structures see Figure S24e-h.

Table S5. Crystal data and structure refinement for **2b**.

	$[Co_2(S_2N_2\text{-cyclam})_2(O_2)(MeCN)_2](OTf)_4$ **2b**
Empirical formula	$C_{30}H_{53}Co_2F_{12}N_7O_{14}S_8$
Formula weight	1338.13
Temperatur (K)	100.00(10)
Radiation	MoKα (λ = 0.71073)
Crystal system	Triclinic
Space group	*P*-1
Unit cell dimensions	
***a* (Å)**	11.5589(13)
***b* (Å)**	14.1698(16)
***c* (Å)**	16.7531(17)
***α* (°)**	89.197(4)
***β* (°)**	72.530(4)
***γ* (°)**	83.298(4)
Volume (Å³)	2598.85
Z	2
Density (calculated) (g/m³)	1.710
Absorption coefficient μ (mm⁻¹)	1.067
F(000)	1368
Crystal size (mm³)	0.14 × 0.19 × 0.67
2θ range for data collection (°)	3.82 to 50.74
Index ranges	-13≤h≤13, -16≤k≤16, -20≤l≤19
Reflections collected	75808
Independent reflections	9241 [R_{int} = 0.088]
Completeness to θ = 50.48 ° (%)	98.4
Absorption correction	multi-scan
Max. and min. transmission	T_{min} = 0.596, T_{max} = 0.745
Refinement method	–
Data/ restraints/ parameters	9241/1411/ 812
Goodness of fit on F^2	1.169
Final R indices [I>2σ(I)]	R_1 = 0.0704, wR_2 = 0.1828
R indices [all data]	R_1 = 0.0932, wR_2 = 0.2007
Extinction coefficient	–
Largest diff. peak and hole (e Å⁻³)	1.18 and -0.55

Table S6. XRD-determined select bond length and bond angle values for the metastable species **2b**, whose molecular structure is showed in the inset.

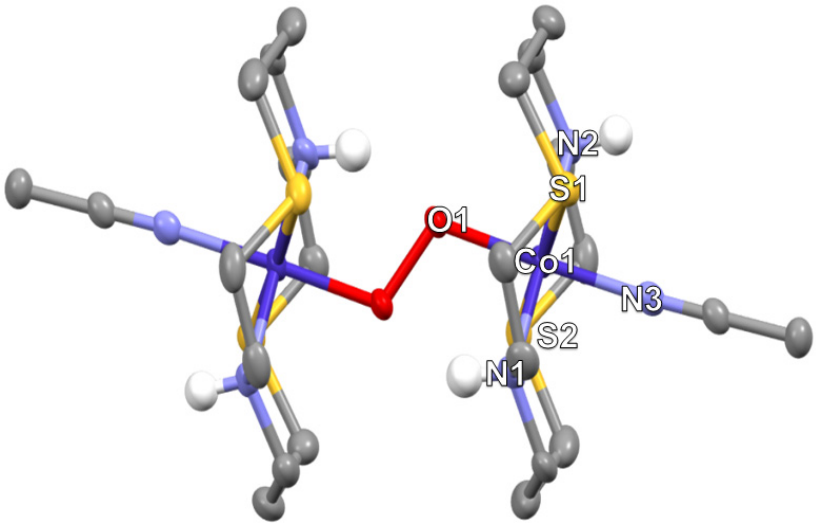

Bond length (Å)			*Bond angle (°)*			
Atom	***Atom***	***r (Å)***	***Atom***	***Atom***	***Atom***	***Angle (°)***
Co1	S1	2.231(2)	S1	Co1	O1	92.5(2)
Co1	O1	1.881(4)	S1	Co1	N1	87.6(2)
Co1	N1	1.984(5)	S1	Co1	S2	178.46(8)
Co1	S2	2.232(2)	S1	Co1	N2	91.3(2)
Co1	N2	2.017(5)	S1	Co1	N3	86.0(2)
Co1	N3	1.942(6)	O1	Co1	N1	90.1(2)
S1	C1	1.810(6)	O1	Co1	S2	88.6(2)
S1	C10	1.802(7)	O1	Co1	N2	89.4(2)
O1	O1	1.508(6)	O1	Co1	N3	178.1(2)
N1	H1	0.81(9)	N1	Co1	S2	93.6(2)
N1	C2	1.49(1)	N1	Co1	N2	178.7(2)
N1	C3	1.502(9)	N1	Co1	N3	90.9(2)
C1	C2	1.50(1)	S2	Co1	N2	87.6(2)
S2	C5	1.808(7)	S2	Co1	N3	92.9(2)
S2	C6	1.810(6)	N2	Co1	N3	89.6(2)
N2	H2	0.81(9)	Co1	S1	C1	95.8(2)
N2	C7	1.50(1)	Co1	S1	C10	105.8(3)
N2	C8	1.497(9)	C1	S1	C10	103.9(4)
N3	C11	1.153(9)	Co1	O1	O1	110.8(3)
C3	C4	1.51(1)	Co1	N1	H1	105(6)
C4	C5	1.52(1)	Co1	N1	C2	113.8(4)
C6	C7	1.49(1)	Co1	N1	C3	118.9(5)
C8	C9	1.52(1)				
C9	C10	1.50(1)				
C11	C12	1.45(1)				
O1	Co1	1.881(4)				
Co1	S1	2.231(2)				
Co1	N1	1.984(5)				
Co1	S2	2.232(2)				
Co1	N2	2.017(5)				

Co1	N3	1.942(6)	
S1	C1	1.810(6)	
S1	C10	1.802(7)	
N1	H1	0.81(9)	
N1	C2	1.49(1)	
N1	C3	1.502(9)	
C1	C2	1.50(1)	
S2	C5	1.808(7)	
S2	C6	1.810(6)	
N2	H2	0.81(9)	
N2	C7	1.50(1)	
N2	C8	1.497(9)	
N3	C11	1.153(9)	
C3	C4	1.51(1)	
C4	C5	1.52(1)	
C6	C7	1.49(1)	
C8	C9	1.52(1)	
C9	C10	1.50(1)	
C11	C12	1.45(1)	
F1	C25	1.33(1)	
F2	C25	1.32(1)	
F3	C25	1.33(1)	
O3	S5	1.429(6)	
O4	S5	1.434(6)	
S5	O5	1.436(6)	
S5	C25	1.826(8)	

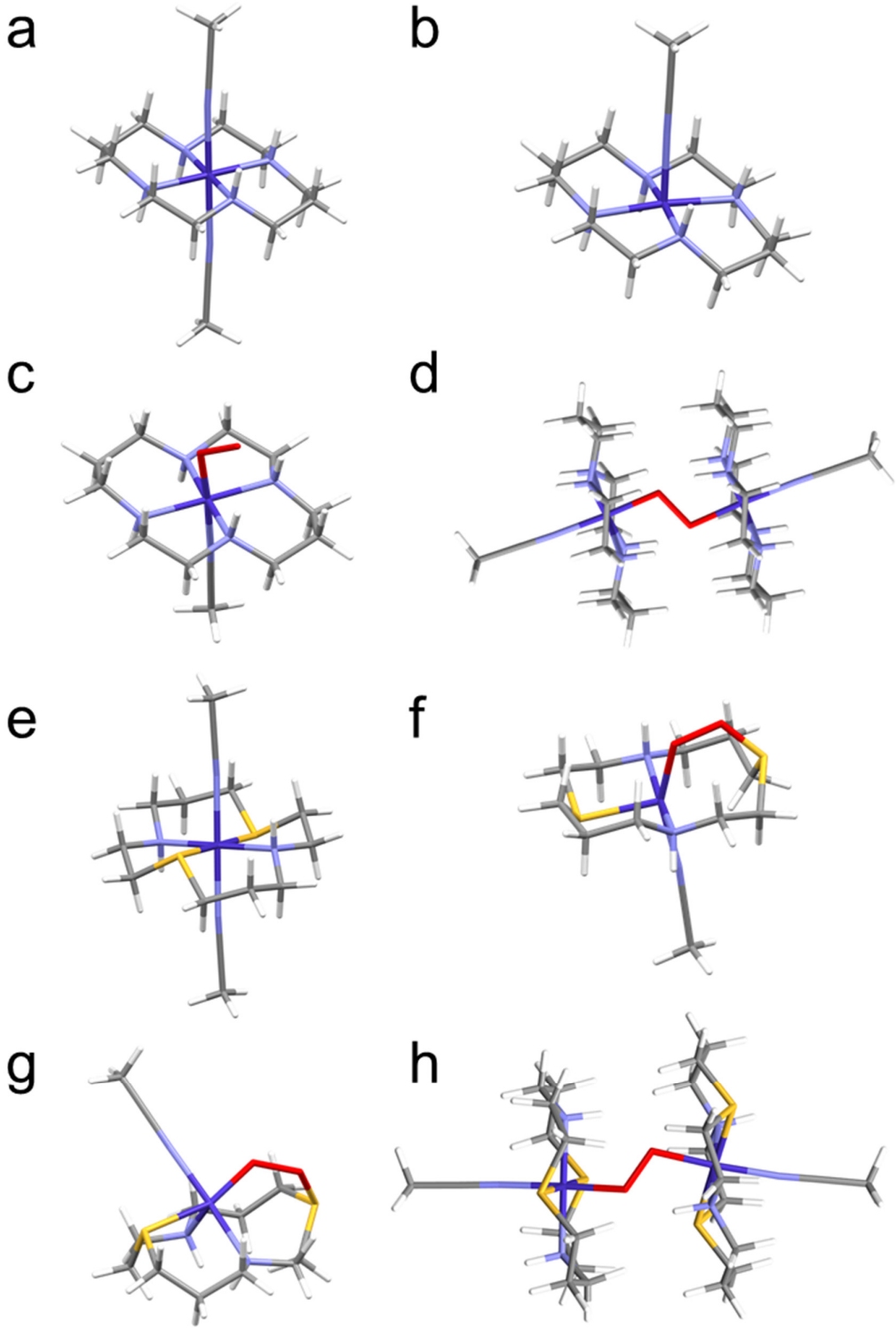

Figure S24. DFT-optimized structures of **1** (**a**), **1'** (**b**), **1a** (**c**), **1b** (**d**), **2** in solvated state (**e**), **2a** *trans* (**f**) and *cis* (**g**) isomers, both in S=3/2 state, and **2b** (**h**).

Table S7. XRD-determined select bond length and bond angle values for the metastable species **[Co(S_2N_2-cyclam)$(TFA)_2$]**.

	[Co(S_2N_2-cyclam)$(TFA)_2$] (2-*cis*)
Empirical formula	$C_{14}H_{22}CoF_6N_2O_4S_2$
Formula weight	519.38
Temperatur (K)	100.00(10)
Radiation	CuKα (λ = 1.54184)
Crystal system	orthorhombic
Space group	Pbca
Unit cell dimensions	
a (Å)	16.3223(4)
b (Å)	14.0169(3)
c (Å)	17.8588(4)
α (°)	90
β (°)	90
γ (°)	90
Volume (Å^3)	4085(16)
Z	8
Density (calculated) (g/m^3)	1.689
Absorption coefficient μ (mm^{-1})	9.234
F(000)	2120.0
Crystal size (mm^3)	0.16 × 0.1 × 0.08
2θ range for data collection (°)	9.68 to 135
Index ranges	-19≤h≤11, -16≤k≤16, -21≤l≤21
Reflections collected	22064
Independent reflections	3671 [R_{int} = 0.0789]
Completeness to θ = 67.5 ° (%)	0.998
Absorption correction	multi-scan
Max. and min. transmission	T_{min} = 0.547, T_{max} = 1.000
Refinement method	–
Data/ restraints/ parameters	3671/ 195/ 290
Goodness of fit on F^2	1.037
Final R indices [I>2σ(I)]	R_1 = 0.0460, wR_2 = 0.1141
R indices [all data]	R_1 = 0.0614, wR_2 = 0.1231
Extinction coefficient	–
Largest diff. peak and hole (e Å^{-3})	0.58 nd -0.44

Table S8. XRD-determined select bond length and bond angle values for the metastable species **[Co(S_2N_2-cyclam)$(TFA)_2$]** , whose molecular structure is shown in the inset.

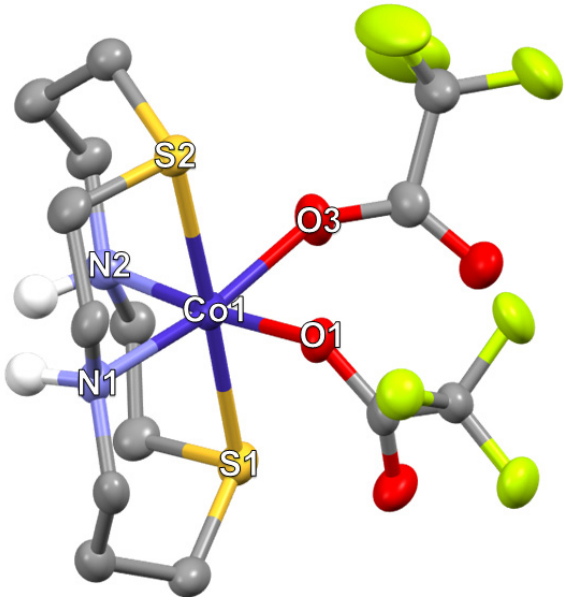

Bond length (Å)			*Bond angle (°)*			
Atom	***Atom***	***r (Å)***	***Atom***	***Atom***	***Atom***	***Angle (°)***
Co1	S2	2.469(1)	S2	Co1	S1	177.85(4)
Co1	S1	2.442(1)	S2	Co1	O1	83.94(7)
Co1	O1	2.058(3)	S2	Co1	O3	86.37(8)
Co1	O3	2.099(3)	S2	Co1	N1	83.98(8)
Co1	N1	2.167(3)	S2	Co1	N2	94.54(8)
Co1	N2	2.160(3)	S1	Co1	O1	98.11(7)
S2	C6	1.820(4)	S1	Co1	O3	94.24(8)
S2	C5	1.818(4)	S1	Co1	N1	95.37(8)
S1	C10	1.814(4)	S1	Co1	N2	83.48(8)
S1	C1	1.809(4)	O1	Co1	O3	90.8(1)
F2	C12	1.350(5)	O1	Co1	N1	88.9(1)
F1	C12	1.335(4)	O1	Co1	N2	174.6(1)
O1	C11	1.269(5)	O3	Co1	N1	170.3(1)
F3	C12	1.346(4)	O3	Co1	N2	83.9(1)
O3	C13	1.237(5)	N1	Co1	N2	96.1(1)
O2	C11	1.216(4)	Co1	S2	C6	110.1(1)
O4	C13	1.240(5)	Co1	S2	C5	96.5(1)
N1	C4	1.483(5)	C6	S2	C5	102.2(2)
N1	C3	1.485(5)	Co1	S1	C10	96.6(1)
N2	C9	1.478(5)	Co1	S1	C1	110.1(1)
N2	C8	1.484(5)	C10	S1	C1	101.7(2)
C11	C12	1.528(5)	Co1	O1	C11	128.8(2)
C2	C3	1.520(5)	Co1	O3	C13	136.0(3)
C2	C1	1.520(6)	Co1	N1	C4	109.1(2)
C13	C14	1.524(6)	Co1	N1	C3	115.2(2)
C9	C10	1.507(5)	C4	N1	C3	109.4(3)
C4	C5	1.522(5)	Co1	N2	C9	110.0(2)

C7	C6	1.512(6)	Co1	N2	C8	118.4(2)
C7	C8	1.528(5)	C9	N2	C8	109.6(3)
C14	F4	1.319(8)	O1	C11	O2	130.6(4)
C14	F5	1.287(8)	O1	C11	C12	111.6(3)
C14	F6	1.372(8)	O2	C11	C12	117.8(3)
			C3	C2	C1	115.5(3)
			O3	C13	O4	130.5(4)
			O3	C13	C14	113.7(3)
			O4	C13	C14	115.7(3)
			F2	C12	F1	106.4(3)
			F2	C12	F3	106.1(3)
			F2	C12	C11	111.6(3)
			F1	C12	F3	106.8(3)
			F1	C12	C11	113.6(3)
			F3	C12	C11	112.0(3)
			N2	C9	C10	109.9(3)
			N1	C4	C5	111.3(3)
			C6	C7	C8	115.7(3)
			S1	C10	C9	108.4(3)
			N1	C3	C2	113.2(3)
			S2	C6	C7	116.0(3)
			S1	C1	C2	116.0(3)
			S2	C5	C4	109.2(3)
			N2	C8	C7	112.9(3)
			C13	C14	F4	114.4(5)
			C13	C14	F5	115.5(5)
			C13	C14	F6	108.8(4)
			F4	C14	F5	109.6(6)
			F4	C14	F6	102.4(6)
			F5	C14	F6	104.9(5)

4. References

[1] G. M. Sheldrick, *SADABS, Empirical Absorption Correction Program*, University Of Göttingen, Germany, **2002**.

[2] G. M. Sheldrick, *Acta Cryst.* **2008**, *A64*, 112–122.

[3] G. M. Sheldrick, *Acta Crystallogr. Sect. A* **2015**, *71*, 3–8.

[4] G. M. Sheldrick, *Acta Crystallogr. Sect. C* **2015**, *71*, 3–8.

[5] C. B. Hübschle, G. M. Sheldrick, B. Dittrich, *J. Appl. Crystallogr.* **2011**, *44*, 1281–1284.

[6] N. Schuth, S. Mebs, D. Huwald, P. Wrzolek, M. Schwalbe, A. Hemschemeier, M. Haumann, *Proc. Natl. Acad. Sci.* **2017**, *114*, 8556 LP – 8561.

[7] H. Dau, P. Liebisch, M. Haumann, *Anal. Bioanal. Chem.* **2003**, *376*, 562–583.

[8] S. Yao, V. Forstner, P. W. Menezes, C. Panda, S. Mebs, E. M. Zolnhofer, M. E. Miehlich, T. Szilvási, N. Ashok Kumar, M. Haumann, K. Meyer, H. Grützmacher, M. Driess, *Chem. Sci.* **2018**, *9*, 8590–8597.

[9] J. J. Rehr, J. J. Kas, F. D. Vila, M. P. Prange, K. Jorissen, *Phys. Chem. Chem. Phys.* **2010**, *12*, 5503–5513.

[10] S. Kundu, F. F. Pfaff, E. Miceli, I. Zaharieva, C. Herwig, S. Yao, E. R. Farquhar, U. Kuhlmann, E. Bill, P. Hildebrandt, H. Dau, M. Driess, C. Limberg, K. Ray, *Angew. Chem. Int. Ed.* **2013**, *52*, 5622–5626.

[11] S. Stoll, A. Schweiger, *J. Magn. Reson.* **2006**, *178*, 42–55.

[12] R. Aasa, tore Vänngård, *J. Magn. Reson.* **1975**, *19*, 308–315.

[13] S. Fukuzumi, K. Okamoto, C. P. Gros, R. Guilard, *J. Am. Chem. Soc.* **2004**, *126*, 10441–10449.

[14] I. Monte-Pérez, S. Kundu, A. Chandra, K. E. Craigo, P. Chernev, U. Kuhlmann, H. Dau, P. Hildebrandt, C. Greco, C. Van Stappen, N. Lehnert, K. Ray, *J. Am. Chem. Soc.* **2017**, *139*, 15033–15042.

[15] A. Paul, R. Borrelli, H. Bouyanfif, S. Gottis, F. Sauvage, *ACS Omega* **2019**, *4*, 14780–14789.

[16] Y. S. Sohn, D. N. Hendrickson, H. B. Gray, *J. Am. Chem. Soc.* **1970**, *92*, 3233–3234.

[17] Z. Halime, H. Kotani, Y. Li, S. Fukuzumi, K. D. Karlin, *Proc. Natl. Acad. Sci.* **2011**, *108*, 13990–13994.

[18] D. Das, Y.-M. Lee, K. Ohkubo, W. Nam, K. D. Karlin, S. Fukuzumi, *J. Am. Chem. Soc.* **2013**, *135*, 2825–2834.

[19] Y.-H. Wang, M. L. Pegis, J. M. Mayer, S. S. Stahl, *J. Am. Chem. Soc.* **2017**, *139*, 16458–16461.

[20] A. Singh, D. R. Chowdhury, A. Paul, *Analyst* **2014**, *139*, 5747–5754.

[21] R. D. Mair, A. J. Graupner, *Anal. Chem.* **1964**, *36*, 194–204.

[22] S. Fukuzumi, S. Kuroda, T. Tanaka, *J. Am. Chem. Soc.* **1985**, *107*, 3020–3027.

[23] K. Mase, K. Ohkubo, S. Fukuzumi, *J. Am. Chem. Soc.* **2013**, *135*, 2800–2808.

[24] N. A. Stephenson, A. T. Bell, *Anal. Bioanal. Chem.* **2005**, *381*, 1289–1293.

[25] Y.-H. Wang, B. Mondal, S. S. Stahl, *ACS Catal.* **2020**, *10*, 12031–12039.

[26] C. Franco, J. Olmsted, *Talanta* **1990**, *37*, 905–909.

[27] C. W. Anson, S. S. Stahl, *Chem. Rev.* **2020**, *120*, 3749–3786.

[28] B. Su, I. Hatay, P. Y. Ge, M. Mendez, C. Corminboeuf, Z. Samec, M. Ersoz, H. H. Girault, *Chem. Commun.* **2010**, *46*, 2918–2919.

[29] J. A. S. Roberts, R. M. Bullock, *Inorg. Chem.* **2013**, *52*, 3823–3835.

[30] A. V Marenich, C. J. Cramer, D. G. Truhlar, *J. Phys. Chem. B* **2009**, *113*, 6378–6396.

[31] A. D. Becke, *J. Chem. Phys.* **1993**, *98*, 5648–5652.

[32] J. P. Perdew, J. A. Chevary, S. H. Vosko, K. A. Jackson, M. R. Pederson, D. J. Singh, C. Fiolhais, *Phys. Rev. B* **1992**, *46*, 6671–6687.

[33] M. J. Frisch, G. W. Trucks, H. B. Schlegel, *Gaussian 16, Revision C.01*, Gaussian, Inc., Wallingford CT, **2016**.

[34] A. Klamt, G. Schüürmann, *J. Chem. Soc. Perkin Trans. 2* **1993**, 799–805.

[35] S. Grimme, J. Antony, S. Ehrlich, H. Krieg, *J. Chem. Phys.* **2010**, *132*, 154104.

[36] R. W. F. Bader, *Atoms in Molecules. A Quantum Theory*, Cambridge University Press, Oxford, U. K., **1991**.

[37] F. Biegler-König, J. Schönbohm, D. Bayles, *J. Comput. Chem.* **2001**, *22*, 545–559.

[38] E. R. Johnson, S. Keinan, P. Mori-Sánchez, J. Contreras-García, A. J. Cohen, W. Yang, *J. Am. Chem. Soc.* **2010**, *132*, 6498–6506.

[39] J. Contreras-García, E. R. Johnson, S. Keinan, R. Chaudret, J.-P. Piquemal, D. N. Beratan, W. Yang, *J. Chem. Theory Comput.* **2011**, *7*, 625–632.

[40] T. Sato, Y. Hamada, M. Sumikawa, S. Araki, H. Yamamoto, *Ind. Eng. Chem. Res.* **2014**, *53*, 19331–19337.

[41] Y.-H. Wang, Z. K. Goldsmith, P. E. Schneider, C. W. Anson, J. B. Gerken, S. Ghosh, S. Hammes-Schiffer, S. S. Stahl, *J. Am. Chem. Soc.* **2018**, *140*, 10890–10899.